SPH modelling of turbulent open channel flow over and within natural gravel beds with rough interfacial boundaries

Ehsan Kazemi[a], Katinka Koll[b], Simon Tait[a], Songdong Shao[a,*]

[a]Department of Civil & Structural Engineering, University of Sheffield, Sheffield S1 3JD, UK
[b]Leichtweiß-Institute for Hydraulic Engineering and Water Resources, TU Braunschweig, Braunschweig, Germany

Abstract

Smoothed Particle Hydrodynamics (SPH) is brought to a level that can be applied to simulate turbulent open channel flows over and within natural porous gravel beds. For this, improvements have been made with regards to i) turbulence modelling, ii) open boundaries (inflow and outflow), and iii) treatment of the rough interface boundary between the porous bed and the overlying free-flow. Flow through the porous bed is simulated macroscopically, and the coefficients of the drag closure model are carefully determined at different layers of the flow; the effect of turbulence is taken into account using a three-layer mixing-length model; and a porous inflow boundary at the inlet as well as an imaginary pressure wall at the outlet are introduced to obtain the required steady and uniform flow conditions. The developed model is then used to simulate eight test cases with two bed conditions, each with four flow conditions. Through the velocity analysis, a nearly S-shaped distribution is observed within the roughness layer for the present test cases. The comparison of the results of the velocity and shear stress with a set of experimental data reveals that the SPH model with the present drag and turbulence closure models as well as the proposed inflow/outflow boundary techniques is capable of simulating complex turbulent channel flows over highly sheared natural porous beds.

Keywords: Porous gravel bed, Interfacial boundary, Inflow and outflow boundaries, Roughness layer, S-shaped velocity profile

1. Introduction

Natural river flows are turbulent and river beds are mostly porous composed of sands and gravels so that water can penetrate and move inside the bed. The momentum transfer at the

*Corresponding author
Email address: s.shao@sheffield.ac.uk (Songdong Shao)

interfacial boundary between porous bed and the adjacent turbulent flow can strongly affect the condition of the overlying flow as well as entrainment and deposition of fine sediments at the bed. Hence, many research studies have been devoted to the development of numerical models, as a complement to experimental studies, to achieve deeper understanding of flow mechanisms and momentum exchange at the interfacial boundary with porous sediment beds.

A mathematical model which is capable of simulating near-bed flows has the advantage of overcoming two limitations with the experimental works on the measurement of flow properties in water-worked armour layers on top of porous sediment beds. The first is the measurement difficulty of approaching all the bed layer locations, and the second is related to the time needed for measuring flow field, which, even for simple armour layers, can take one week using a three-dimensional Laser Doppler Anemometry (3D-LDA) probe, excluding the time needed for initially developing the armour layer. Hence, with an advanced numerical modelling technique, not only the entire near-bed flow field can be solved, but also the complex features of the rough bed can be researched more easily.

There are two general approaches in the mathematical modelling of flow through porous media, i.e. microscopic and macroscopic approaches. In the microscopic representation of the media, the fluid-solid interfaces are modelled as rigid no-slip boundaries either in a Direct Numerical Simulation (DNS) with resolving all scales of fluid flow or using a Large Eddy Simulation (LES) in which only those scales above a threshold are resolved. In the macroscopic approach, the media is represented as single-phase continua and the frictional effects of the solid matrix are incorporated as extra stress terms in the governing equations in order to produce the required balance in the momentum.

Breugem and Boersma (2005), Stoesser et al. (2007), Fang et al. (2018), Leonardi et al. (2018) and Lian et al. (2019) are some examples of microscopic modelling of porous media in the simulations of turbulent channel flows over porous walls. The first one was based on DNS while the others applied LES. DNS is advantageous due to the amount of information it provides. However, it is computationally costly thus limited to low Reynolds (Re) number flows. As an alternative, LES is used to resolve a certain range of flow scales at a lower cost while the unresolved part is modelled using an appropriate turbulence closure model such as Sub-Grid-Scale (SGS) model. In all above-mentioned microscopic studies, homogeneous porous media composed of arrays of cubes or spheres were simulated. Microscopic modelling of natural porous beds is difficult as the microstructure of the solid matrix is either unknown or difficult to be represented in the model. Therefore, porous natural beds are often modelled macroscopically.

In macroscopic modelling, a set of spatially averaged governing equations are solved. These equations are obtained by applying a spatial filter to the microscopic equations over a small averaging volume so that extra stress terms, representing the frictional effect of solid skeleton on the average flow field, emerge in the governing equations. In this approach also, DNS or LES can be applied to account for the flow turbulence, although the latter is more commonly documented.

Due to the averaging process, dealing with the interfacial boundary between porous media and an adjacent fluid flow is difficult. The interfacial boundary under a turbulent condition is usually highly sheared with rapid change of flow properties over a thin layer. This layer cannot be easily treated using the averaging process in macroscopic modelling. This is one reason that some researchers have used a step change (namely, 'jump') in their mathematical representations of the interfacial boundary. For example, in their macroscopic DNSs of turbulent channel flows over permeable walls, Hahn et al. (2002) used a discrete step change in velocity, and Rosti et al. (2015) applied a momentum transfer condition with a stress jump, at the interface. However, continuous interfacial boundary layers have also been successfully applied in some studies with high gradient interfacial boundaries, such as the works done by Breugem et al. (2006). In the continuous interface approach, a unified computational domain is employed for all regions including the porous media and free-flow (clear water), with a continuity of flow properties at the interfacial boundary, while the change in the characteristics of different regions is addressed by applying different numerical parameters and/or closure models. Macroscopic modelling of porous media with a continuous interfacial boundary has particularly been more attractive in particle modelling approaches recently developed for flow interaction with porous media due to its robustness and ease of implementation in the Lagrangian framework.

Particle methods such as the Smoothed Particle Hydrodynamics (SPH) and Moving Particle Semi-implicit (MPS) methods have been widely used for simulation of fluid flows in various fields, with some recent advances in pressure calculation (Wang et al., 2019), turbulence modelling (Di Mascio et al., 2017), energy conservation (Khayyer et al., 2017b), wall boundary condition (Leroy et al., 2014), open boundary conditions (Hu et al., 2019), sediment transport and morphological dynamics (Ghaitanellis et al., 2018; Harada et al., 2018), δ-SPH (Meringolo et al., 2018), and Particle Shifting (PS) technology (Khayyer et al., 2017a). For more details on the state-of-the-art of particle methods refer to Gotoh and Khayyer (2018).

Recently, particle methods have been employed successfully in the macroscopic simulation of fluid flow interaction with porous media. Except for the study of Shao (2010), where the porous and free-flow regions were separated and matching conditions of velocity and stresses were imposed at the interface boundary line, other studies such as Akbari and Namin (2013), Akbari (2014), Ren et al. (2014), Gui et al. (2015), Ren et al. (2016), Pahar and Dhar (2016), Pahar and Dhar (2017), Khayyer et al. (2018) and Kazemi et al. (2019) applied continuous interfacial boundary at the interface. All these models were developed to study wave interaction with porous structures where the interface was often supposed to be smooth and the flow near the interfacial boundary was not highly sheared.

To the best of the authors' knowledge, there has been no SPH study on the modelling of turbulent open channel flows over natural porous beds. In addition to the difficulty with the treatment of the rough interfacial boundary with regards to the determination of drag and turbulence effects, dealing with inflow and outflow boundaries in such problems is also difficult. This is due to the Lagrangian nature of the method since the computational domain contains two regions with completely different characteristics, i.e. the porous and free-flow regions, with a high gradient interfacial boundary between them. Some examples of the SPH inflow/outflow boundary techniques are found in Federico et al. (2012), Aristodemo et al. (2015), Kazemi et al. (2017) and Hu et al. (2019) which were all developed for channel flows over impermeable beds or laminar flow condition.

In the present study, an SPH macroscopic model with a continuous interfacial boundary is developed for simulating turbulent open channel flows over natural gravel beds. With the objectives of careful treatment of the turbulence and frictional effects in different flow layers (i.e. the porous, roughness, and free-flow layers), development of appropriate inflow and outflow boundary techniques to achieve steady and uniform conditions within a short-length computational domain in the presence of an interfacial boundary where the flow properties change rapidly, and a detailed analysis of velocity profiles in the roughness layer, the present study investigates momentum transfer mechanisms in the context of SPH, which unlocks the capacity of this method in modelling turbulent channel flows over and through rough porous beds, which can eventually pave the way towards modelling sediment transport in natural river condition by particle methods.

2. Case Study

A set of existing experimental data of turbulent flow over porous sediment layer with two different bed conditions and several flow discharges is employed to be simulated and validate the model results. A brief description of the experimental study is presented in the following. For more details see Aberle (2006), Aberle (2007) and Aberle et al. (2008).

The experiments were carried out in the laboratory of the Leichtweiss-Institute for Hydraulic Engineering, Technical University of Braunschweig, in a tilting flume with a constant slope S_0 of 0.0027. The length, width and height of the flume were 20 m, 0.90 m and 0.60 m, respectively. A mixture of coarse gravel sediments (0.63 to 64 mm) was placed in the bottom of the flume. Several bed conditions were tested, each with several flow discharges, i.e. several beds were formed by different flow rates and then, each of them was subject to a range of flow conditions. The procedure was that an armouring discharge was firstly run into the flume, mobilising the sediment, and then maintained until the bed surface reached stable condition, i.e. the sediments stopped moving. For this bed, then, several measuring discharges Q less than the armouring discharge Q_{armour} were run into the flume and flow velocity was measured using a 3D Laser Doppler Anemometer (LDA) system at 24 vertical profiles distributed randomly in the test section, which was located 9 m downstream of the flume inlet. The test section was 2.40 m long and 0.36 m wide. Its width was smaller than the total flume width to reduce side wall effects. In all experiments conducted with the measuring discharges less than the reference armouring discharge, the bed material was immobile, and the flow was steady and uniform. This procedure was repeated for several armouring discharges (i.e. bed conditions).

Fig. 1 depicts a 2D schematic side view of the flume including porous sediment layer, free-flow (clear water), and roughness (interfacial) layer. In the figure, z_b is the level of the rigid wall at the bottom of the flume; z_t and z_c show trough and crest of the roughness layer, respectively; z_m is equal to z_t plus the equivalent height of the roughness (i.e., the volume of melted roughness materials per unit bottom area); z_{ws} represents the water surface level; and H_p, Δ_s and H_c denote the thickness of the porous sediment layer, roughness layer and free-flow, respectively. Every time with applying a new armouring discharge, z_t, z_m and z_c levels changed, while the change in the bed material below z_t was supposed to be very small.

For each experiment, the double-averaged velocity and Reynolds Stress profiles in the roughness and free-flow layers were estimated by spatially averaging the time-averaged profiles on planes parallel to the bed level over the 24 measuring locations. Within the roughness layer, all 24 measuring points were not available at some planes due to the existence of solid material. Therefore, the averaging was carried out from the levels with at least five available points. Some earlier results of the hydraulic measurements can be found in Aberle (2006) and Nikora et al. (2007b).

Simulation of this problem with a numerical model is particularly challenging since the interface is rough and has a considerable thickness so that the flow structure inside the roughness layer significantly affects the flow both above and below it, thus, in addition to the porous and free-flow regions, careful consideration is also required for the treatment of flow within this layer. In the present study, the experiments of bed conditions corresponding to the armouring discharges $Q_{\text{armour}} = 180$ l/s and 250 l/s, namely beds B1 and B2, are selected to be simulated. For bed B1, the tests with measuring discharges of 90, 120, 150 and 180 l/s; and for bed B2, the tests with measuring discharges of 90, 150, 220 and 250 l/s are considered. Table 1 represents some details of the bed and flow conditions of the test cases. It is noted that the vertical levels (z_t, z_c and z_{ws}) are measured from an arbitrary reference.

3. Governing Equations and Model Closures

The SPH-Averaged Macroscopic (SPHAM) equations of mass and momentum (Kazemi et al., 2019) are considered as the governing equations for the present simulations. The discretised form of these equations is presented in Eqs. (1) and (2). These equations are defined in a unified framework, i.e. they describe the fluid motion over the entire computational domain including porous, roughness and free-flow regions. The continuity of flow properties over the interfacial boundary is naturally satisfied. The model is based on the Weakly Compressible SPH (WCSPH) method where the equation of state is used to link the mass and momentum equations for calculation of pressure as presented in Eq. (3), which is written in terms of intrinsic average of fluid density (but not the volumetric density of SPH particles), thus applicable in all regions, i.e. free-flow, roughness and porous sediment layers (Kazemi et al., 2019). The temporal change in the fluid density is restricted to be less than 1% by choosing an appropriate value for the speed of sound (c_0) to ensure the incompressibility of the flow. The predictor-corrector method is employed for time implementation.

$$\frac{\rho_a^{t+\Delta t} - \rho_a^t}{\Delta t} = \sum_b \frac{m_b}{\phi_a \phi_b} \left(\phi \mathbf{u}\right)_{ab} \nabla_a W_{ab} \tag{1}$$

$$\begin{aligned}\frac{\mathbf{u}_a^{t+\Delta t}-\mathbf{u}_a^t}{\Delta t} &= -\sum_b \frac{m_b}{\phi_b}\nabla_a W_{ab}\frac{P_a+P_b}{\rho_a\rho_b}+\mathbf{g}\\ &+\sum_b \frac{\mu m_b}{\phi_a\phi_b}\frac{\mathbf{r}_{ab}\cdot\nabla_a W_{ab}}{\left|\mathbf{r}_{ab}\right|^2}\frac{\phi_{ab}\mathbf{u}_{ab}+2\left(\phi\mathbf{u}\right)_{ab}}{\rho_a\rho_b}\\ &-\sum_b \frac{m_b}{\phi_b}\nabla_a W_{ab}\frac{\phi_a\boldsymbol{\tau}_a+\phi_b\boldsymbol{\tau}_b}{\rho_a\rho_b}-\mathbf{A}_a\end{aligned} \tag{2}$$

$$P_a = {c_0}^2\left(\rho_a-\rho_{0,a}\right) \tag{3}$$

where $\mathbf{r}_{ab} = \mathbf{r}_a - \mathbf{r}_b$; $\mathbf{u}_{ab} = \mathbf{u}_a - \mathbf{u}_b$; $\phi_{ab} = \phi_a - \phi_b$; $(\phi\mathbf{u})_{ab} = \phi_a\mathbf{u}_a - \phi_b\mathbf{u}_b$; and $\nabla_a W_{ab} = \nabla_a W\left(\mathbf{r}_a - \mathbf{r}_b, h\right)$. Subscripts a and b denote the central particle in the averaging volume (averaging area, in 2D) and its neighbouring particles, respectively; W is the kernel function; h is the smoothing length; and $\mathbf{r}$ denote the particle's position. m, ρ and P are fluid mass, density, and pressure; ϕ is porosity; $\mathbf{u}$ is the intrinsic average of velocity; $\mathbf{g}$ is the gravitational acceleration; $\boldsymbol{\tau}$ is the turbulent shear stress tensor; and $\mathbf{A}$ is a drag-induced shear stress term. The effect of porosity on the particle's apparent density is taken into account in the equations, so that the particle spacing changes when it travels into regions with different porosities. The last two terms in the momentum equation represent the effects of turbulence and friction of solid skeleton of the porous media on the macroscopic flow field, respectively, which will be determined through the closure models in Sections 3.2 and 3.3.

The discretised forms used for all the derivatives in the momentum equation conserve the linear momentum (in the absence of external forces), but the viscosity and turbulent stress terms (the third and fourth terms on the right-hand side of Eq. (2)) do not conserve the angular momentum due to the anisotropic shear stress tensors, since the angular moment between a pair of particles vanishes only if the internal stress tensor is isotropic (Khayyer et al., 2008). To resolve this issue, the correction of Khayyer et al. (2008) can be applied into the kernel gradients, thereby enforcing preservation of angular momentum for viscous internal forces. Khayyer et al. (2008) stated that in SPH simulation, preservation of angular momentum is necessary for the cases with violent free surface deformations such as breaking of water waves. Although those large surface deformations are not usually observed in water flows in porous media, correcting kernel gradients as carried out by Khayyer et al. (2008) can enhance the computational efficiency.

The present form of the pressure gradient and turbulent shear stress terms (the first and fourth terms on the right-hand side of Eq. (2)) is a similar derivation of the stable form used in many SPH studies for gradient and divergence terms (e.g. Shao and Lo, 2003; Khayyer et al., 2008). However, as Khayyer et al. (2017b) pointed out, this form guarantees the Taylor series consistency only if particles are regularly distributed in a compact kernel support (which is not the case for free surface flows). As a remedy, the PS technology has been developed and used in several studies (e.g. Khayyer et al., 2017a) to achieve regular distributions of particles, thereby mitigating the Taylor series inconsistency. Application of a Taylor series consistent pressure gradient is especially important for improving the energy conservation feature of the numerical solution. The efficiency of the present scheme in the conservation of energy can be investigated in a future study by checking the evolution of kinetic and potential energy components in the simulation of a conserved system such the long-term evolution of a standing wave as presented in Antuono et al. (2015) and Khayyer et al. (2017b).

3.1. Determination of porosity

In the experiments, the laboratory flume was filled by water and the porosity was estimated as the volume of fluid the porous layer contains divided by the total volume of the layer. It was observed that the solid material at the interface had significant changes under different armouring discharges while it remained unchanged below the roughness trough z_t. Therefore, it is assumed that the mean porosity ϕ is constant below z_t and is equal to the average porosity of the sediment layer, i.e. $\phi_0 = 0.22$, for all bed conditions. However, the distribution of porosity within the roughness layer (from z_t to z_c) needs to be defined for each bed condition (B1 and B2 in Table 1). The simplest definition could be a linear profile from roughness trough z_t with the value of ϕ_0 to the roughness crest z_c with a value of 1.0. However, it is noted that z_t and z_c are the absolute lower and higher levels of the roughness layer where the density of solid material may have a smaller change near these levels compared to its variation in the middle of the roughness layer. Therefore, it is assumed that the most part of the variation of porosity occurs in a layer (namely, porosity interface layer) in the middle of the roughness layer as depicted in Fig. 1 by red dash-dotted lines. In a typical rough surface, the physical distribution of the solid material density is often unknown, so the thickness of the porosity interface layer as well as the type of porosity variation over this layer should be reasonably assumed. According to some computation trials, the porosity interface layer is assumed to have a thickness of $0.5\Delta_s$ with a centre at z_m. Besides, the porosity variation over this layer is supposed to be linear. According to this definition, a typical distribution of porosity over the total depth in the numerical model is presented by the red solid line in Fig. 1. This profile is used to determine the porosity of particles based on their elevation. In order to impose a smooth change from the linear profile to the constant values at the lower and upper bounds, a Spline function with supports of, respectively, r_t and r_c is employed to smooth out the profile. r_t and r_c may have slightly different values as the centre of the porosity interface layer z_m may not be exactly at the centre of the roughness layer, i.e. $z_m \neq z_t + 0.5\Delta_s$.

3.2. Determination of the frictional effect of solid material

The last term added to the momentum equation, $\mathbf{A}_a$, represents the viscous and form-drag effects of solid skeleton on the macroscopic flow field at particle a. These effects have been estimated using various drag closure models in the literature. In the simulations carried out by Kazemi et al. (2019), it was shown that the application of Ergun's closure equation with its original coefficients provides good accuracy for flow through porous media in different civil engineering applications. Ergun's equation has been obtained from measuring various flow conditions in packed beds. In the present study, the sediment layer below the roughness trough level z_t is assumed to be well packed so that the Ergun's equation is applied for the bed from z_b to z_t as follows

$$\mathbf{A}_a = -c_1 \frac{(1-\phi_a)^2}{{\phi_a}^2} \frac{\nu_0}{{d_s}^2} \mathbf{u}_a - c_2 \frac{(1-\phi_a)}{\phi_a} \frac{1}{d_s} \mathbf{u}_a |\mathbf{u}_a| \tag{4}$$

where ν_0 is the fluid kinematic viscosity coefficient; c_1 and c_2 are the viscous and form-drag coefficients equal to 150 and 1.75, respectively, according to Ergun (1952); and d_s is the bed mean particle size which is assumed to be equivalent to d_{50} of the bed material in the present study.

Observing the experimental data, particularly bed topography scans (Aberle, 2007; Aberle et al., 2008), it is found that the bed is not packed within the roughness layer, but with considerable spacing between solid particles. In fact, within this layer, the drag interaction is rather between flow and single (or few) particles so that the application of Ergun's equation may be inaccurate. Therefore, the drag force model introduced in Kazemi et al. (2017) is applied here with some modifications for the estimation of $\mathbf{A}_a$ within the roughness layer.

According to Kazemi et al. (2017), the cross-sectional area A_d and the bed-parallel planar area A_τ in their Eqs. (11) and (12) are equivalent to the fluid particle size l_0 and the product of $d_s l_0$, respectively. Moreover, the shape function W_d can be replaced by $(1-\phi)$ which represents the density distribution of solid phase within the roughness layer. Therefore, the form-induced shear stress term within the roughness layer is formulated as

$$\mathbf{A}_a = -C_d\,(1-\phi_a)\,\frac{1}{d_s}\mathbf{u}_a|\mathbf{u}_a| \tag{5}$$

where C_d is the drag coefficient which is taken to be 0.9 for natural roughness particles, according to the study of Schmeeckle et al. (2007). By using this equation, the effect of viscous drag is neglected within the roughness layer, which should not be invalid in the present simulations due to the fact that in high Re number flows, form-induced drag is dominant. Combining Eqs. (4) and (5) yields the following relationship for $\mathbf{A}_a$ over the entire domain including the porous sediment layer, the roughness layer, and the free-flow region.

$$\begin{aligned}\mathbf{A}_a = &-\alpha_v\frac{(1-\phi_a)^2}{{\phi_a}^2}\frac{\nu_0}{{d_s}^2}\mathbf{u}_a - \alpha_d\frac{(1-\phi_a)}{\phi_a}\frac{1}{d_s}\mathbf{u}_a|\mathbf{u}_a| \\ &: \begin{cases} \alpha_v = 0, \alpha_d = C_d\phi_a & : \quad z_t < z \leq z_c \\ \alpha_v = c_1, \alpha_d = c_2 & : \quad elsewhere \end{cases}\end{aligned} \tag{6}$$

where ϕ_a is estimated using the procedure introduced in Section 3.1. The calculated drag term will be zero in the free-flow region where the porosity is equal to 1.0, and have a smooth transition near the lower and upper limits of the roughness layer (z_t and z_c) due to the smooth transitions in the porosity and velocity at those boundaries.

The drag term $\mathbf{A}_a$ added to the momentum equation (Eq. (2)) acts as external body force on fluid particles. This term was emerged as a surface integral in the SPHAM equation of momentum through the averaging process of the equation (refer to Kazemi et al., 2019), and then approximated by closure models based on concepts from the hydraulic point of view. This form is different from the one applied in some studies, e.g. Khayyer and Gotoh (2010), where radial and anti-symmetric inter-particle forces between a fluid particle and its neighbouring wall particle was the basis of the definition of the drag term in the momentum equation. In the present macroscopic description of the porous media, fluid-solid interfaces are not modelled as rigid wall boundaries, i.e. only fluid particles exist in the domain where the frictional effect of solid material is modelled macroscopically.

3.3. Determination of the effect of turbulence

In the macroscopic modelling of the porous media, as it is described as continua, i.e. the physical geometry of the solid skeleton is not modelled, the physical dispersion which is a result of flow obstruction by solid particles is disregarded. Kazemi et al. (2017) showed that for SPH macroscopic modelling of turbulent flows over rough beds, the Sub-Particle-Scale

(SPS) model of Gotoh et al. (2001) can be applied, but with a modification to the estimation of the eddy viscosity. They employed a mixing-length model based on the mixing-length formula of Nezu and Rodi (1986), instead of using the standard Smagorinsky model, and successfully simulated the depth-limited turbulent flows over rough beds of packed spheres, macroscopically. In the present study, their mixing-length model is modified to include the turbulence effects in the porous sediment and roughness layers too, by introducing a three-layer mixing-length model as the following. It will be shown in Section 5, with evidence, why the SPS model with the standard Smagorinsky coefficient will not work in the macroscopic simulation of a rough interface and an alternative approach such as the present mixing-length model is necessary.

Thanks to the availability of the detailed velocity and Reynolds Stress data to some distance below and above the roughness crest z_c, the experimental mixing-length was estimated as $l_m = \sqrt{\frac{\tau_{\exp}}{\rho(\partial u/\partial z)^2}}$ (in which $\tau_{\exp} = \rho\overline{u'w'}$ is the Reynolds Stress derived from the experimental velocity data where u' and w' are the temporal fluctuations of the streamwise (x) and vertical (z) components of the experimental velocity, and the overbar denotes the temporal averaging operator), and then compared with the formula of Nezu and Rodi (1986) for the present test cases. A good agreement was observed for all the test cases by adopting the value of 0.22 for the slope of the mixing-length profile κ_f (see Fig. 2). Therefore, Nezu and Rodi (1986) formula is employed to estimate the mixing-length l_m above the roughness layer (from roughness crest z_c to water surface z_{ws}) with $\kappa_f = 0.22$ and a certain reference value at z_c which is dependent on the mixing-length distribution within the roughness layer.

Determination of the mixing-length distribution within the roughness and lower sediment layers is not straightforward since the data is available only to some distance below the roughness crest z_c, but not within the bed. It was observed that the mixing-length is linear at the upper part of the roughness layer with a certain slope κ_r, which is different from κ_f. The data is not available in the lower part, but it is assumed that l_m has a linear distribution over the lower part too, with the same slope of κ_r. It was found that κ_r is about 0.27 and 0.15 for the bed conditions B1 and B2, respectively.

Using these values, the linear profiles (fitted to the experimental data) become zero at some levels about 10 mm above z_t and about 0 to 20 mm below z_t for the test cases associated with the beds B1 and B2, respectively. However, the mixing-length is not physically zero within the bed, although flow turbulence may be negligible in that region. Therefore, it is assumed that the mixing-length profile is fixed at a certain level z_0, below which it has a constant value of l_{mb}. z_0 has a vertical distance of Δz_0 from the roughness trough.

According to the above investigations, the following equation is defined to be used for the estimation of the mixing-length distribution in the depth-wise direction from the flume rigid bottom wall z_b to the water surface z_{ws}. Fig. 2 illustrates this distribution schematically.

$$
\begin{aligned}
l_m &= l_{mb} && : z \leq z_0 \\
l_m &= l_{mb} + \kappa_r \left(z - z_0\right) && : z_0 < z \leq z_c \\
l_m &= l_{mb} + \kappa_r \left(z_c - z_0\right) && \\
&\quad + \kappa_f \left(z - z_c\right) \sqrt{1 - \left(z - z_c\right) / H_c} && : z > z_c
\end{aligned}
\tag{7}
$$

Considering the fact that l_{mb} represents the turbulent length scale within the porous sediment layer, a small value in the order of one-tenth of the average size of solid particles should be sufficient. A value of $l_{mb} = 2$ mm is considered in the present study. Using this value, Δz_0 will be about 18 to 23 mm and -10 to 10 mm for beds B1 and B2, respectively. Thus, the averages of these values are employed for Δz_0. Table 2 summarises the values applied in the present simulations.

It should be noted that the mixing-length profiles extracted from the experimental data are not directly used in the numerical simulations, but the data is used to derive the generalised form in Eq. (7) depicted in Fig. 2. This profile is then used in the simulation of the test cases with calibrations for each bed condition, as presented in Table 2. It is suggested that the general form proposed in this study can be used for similar applications, with proper calibrations when different bed conditions are simulated.

4. Computational Domain and Boundary Conditions

2D simulations are carried out with the computational domain set up based on the physical model introduced in Section 2. Due to the limited computational power, the same experimental flume length (20 m) is not possible to be applied here, thus a shorter domain (4 m) is considered, and uniform and steady flow conditions are achieved within this length with the aid of the inflow and outflow boundary techniques proposed in the following sections. Besides, the dynamic boundary condition (Dalrymple and Knio, 2001) is applied for the bottom rigid wall at the level z_b, while the free surface boundary is tracked without any special treatment.

4.1. Inflow boundary

Several layers of dummy particles are set in the inflow region in order to address the truncated support area of the particles in the inner-fluid region (see Fig. 3). The governing equations are not solved at these inflow dummy particles but their properties such as pressure and velocity are determined based on the desirable hydraulic conditions. They move according to their velocity and become fluid particles when passing the inflow boundary line (X^{in}), while a new inflow dummy particle with the same properties is generated at the same elevation but in the beginning of the inflow region, i.e. at the inlet threshold.

This type of inflow boundary treatment has been used in several SPH studies such as Federico et al. (2012) and Kazemi et al. (2017). However, based on our trials, this approach will not work for the present problem due to the existence of two different flow layers, i.e. the porous sediment and the free-flow layers, especially with rapid variations of flow properties at the rough interface. Therefore, here, we propose using a porous inflow boundary with a porosity between that of those two layers, i.e. between ϕ_0 and 1.0, with a transition zone from the inflow boundary to the area with the prescribed porosity profile depicted in Fig. 1.

Fig. 3 shows the inflow setup at the initial time and the change of porosity from the inflow boundary to the inner fluid domain. Porosity within the inflow region and to some small distance away from the boundary (i.e. in the constant ϕ zone) is set to a constant value ϕ^{in}; and after that, it changes gradually (linearly here) from X_1^{tr} to X_2^{tr} and reaches the required value beyond X_2^{tr} (which is equal to ϕ_0, 1.0, and some value between these two, respectively, in the porous bed, free-flow region and roughness layer). The constant ϕ zone is applied for a smooth and stable transformation of flow at the inlet. In the present simulations, as a porosity between ϕ_0 and 1.0 is chosen for the porous inflow region, a depth higher than the desirable one (experimental depth) is set at the inlet in order to have a stable solution, i.e. $z_{ws}^{in} > z_{ws}$. The depth H_t^{in} and the porosity ϕ^{in} can be determined by numerical trials so that a stable flow condition is achieved within the shortest possible length of the transition zone; then a constant inflow velocity is determined according to the desired flow discharge (measuring discharge in Table 1), calculated as $U^{in} = q^{in}/\phi^{in} H_t^{in}$, where q^{in} is the discharge per unit width which is equal to Q/B_w with Q and B_w being the measuring volume discharge and the flume width at the measuring section, respectively. Besides, the pressure of the inflow particles is considered to be hydrostatic. In this way, the inflow region acts as a porous medium where water flows into the domain with a constant rate.

For the porous area between X^{in} and X_2^{tr} Ergun's constants are used for the estimation of $\mathbf{A}_a$, so that the range in Eq. (6) is modified as $\alpha_v = 0$, $\alpha_d = C_d \phi_a$ for $x > X_2^{tr}, z_t < z \leq z_c$; and $\alpha_v = c_1$, $\alpha_d = c_2$ elsewhere.

It is expected that the flow depth decreases gradually over the transition zone and reaches a constant depth beyond X_2^{tr}. The final depth depends on various factors such as bed roughness, slope, and turbulence intensity.

4.2. Outflow boundary

Since the computational length is short ($8H_t^{in}$ in the present simulations), an open outflow boundary could not satisfy the required uniform flow condition within the domain. Here, an outflow boundary technique (similar to the one proposed by Shakibaeinia and Jin (2010) although with different applications) is proposed to overcome this difficulty.

Due to a truncated domain at the outlet boundary, the balance in the momentum equation is disturbed so that the water column collapses if no special treatment is applied. On the other hand, if one uses several layers of dummy particles beyond the outlet boundary, as in the inflow region, to recover the truncated kernel area of the fluid particles, there will still be a problem in defining flow quantities at those dummy particles. Hence, a simple outflow boundary technique is proposed by introducing a pressure gradient in the opposite direction of the streamwise flow thereby reproducing a constant depth which yields the required uniform flow condition within a short distance from the boundary. For this purpose, an imaginary wall is placed at the outlet which provides only pressure gradient on the fluid particles as described in the following.

Several layers of fixed imaginary particles are set beyond the outlet line X^{out}, as in Fig. 4, in order to create an imaginary wall with a certain height (H_{ow}) and a certain distribution of pressure. A hydrostatic pressure distribution is considered in the present simulations. The imaginary particles contribute only in the calculation of pressure gradient at the fluid particles. Therefore, the following term is added to the momentum equation (Eq. (2)) of a certain fluid particle a when it is located within a distance shorter than $2h$ from the outlet boundary line (see Fig. 4(b)).

$$\Xi_a = -\sum_o \frac{1}{\rho_a} F_o \Delta V_o \nabla_a W_{ao} \left(P_a + P_o\right) \tag{8}$$

where a and o denote the fluid and its neighbouring imaginary particles, respectively; ΔV_o is the volume of the imaginary particle; and F_o is a relaxing factor used to ensure that the fluid particles will move smoothly towards the (fixed) imaginary wall, with the conservation of mass being preserved. In the present simulations, a linear formulation is employed as $F_o = (X^{out} - x_a)/2h$, where x_a is the horizontal position of the fluid particle approaching the boundary line. In fact, adding F_o into Eq. (8) allows that the volume of the neighbouring imaginary particles of the fluid particle a, i.e. ΔV_o, decreases gradually when particle a is approaching the outlet boundary line and eventually becomes zero when particle a reaches the boundary line. In this way, the fluid particles move smoothly towards the imaginary wall while experiencing a hydrostatic pressure gradient in the opposite direction, and are then removed when they pass X^{out}.

Fig. 4(a) shows the initial set-up of the particles at the outlet and Fig. 4(b) depicts a generic fluid particle a approaching the imaginary wall. The height of the imaginary wall is lower than the initial water depth, however, the difference becomes small after the development of the flow (see Fig. 5). It can be seen from Fig. 4(a) that a larger particle spacing is initially set in the region of the porous sediment layer. This is to accelerate the achievement of the steady-state due to the fact that, according to the governing equations, the particle spacing will get larger in the areas with lower porosity.

By considering a hydrostatic pressure distribution, neglecting the effect of other terms such as viscosity in the calculation of Ξ_a, and using a linear relaxing factor for mass elimination at the outlet boundary, the outflow boundary treatment may not guarantee an exact balance in the flow momentum at the outlet. Therefore, the height of the imaginary wall H_{ow} is considered to be adjustable in order to be able to get the depth constant within the fluid domain thereby providing the required uniform condition. For each test case, H_{ow} is adjusted so that the water surface becomes parallel to the bed line. In addition, the depth-averaged streamwise velocity is compared at several sections within the fluid domain, and if the difference is less than a threshold, flow is considered as uniform.

5. Results and Discussion

The eight test cases introduced in Table 1 are simulated using the developed model. A rectangular computational domain is adopted with the initial height and length of H_t^{in} and $8H_t^{in}$. The domain is discretised using particles with clear water particle spacing l_0 of 5 mm. The cubic Spline function (Monaghan and Lattanzio, 1985) is employed and the smoothing length is chosen to be $1.2l_0$. The CFL condition with the coefficient of 0.125 is adopted for the time step size, and a Shepard density filter is applied at every 30 time steps to reduce the pressure error due to the spatial density variations.

At the inflow boundary, ϕ^{in} and H_t^{in} are set to 0.75 and $H_p + 1.5\,(z_{ws} - z_t)$, respectively, where H_p is the thickness of the porous armour layer (see Fig. 1). Accordingly, the inflow velocity is computed as discussed in Section 4.1 and the inflow pressure distribution is assumed to be hydrostatic. The number of layers of the inflow dummy particles is set to three. X_1^{tr} and X_2^{tr} are set to $X^{in} + H_c$ and $X^{in} + 4H_c$, respectively (see Fig. 1 for H_c). These values are determined by numerical trials to achieve stable flow conditions within the shortest possible length of the transition zone. At the outflow boundary, three layers of imaginary particles are placed beyond the outlet boundary line (X^{out}) to construct the imaginary wall. The spacing between those particles is set to the clear water particle spacing l_0 so that ΔV_o is equal to l_0^2 and their porosity is 1.0.

5.1. Flow steadiness and uniformity

Figures 5 and 6 present snapshots of the streamwise velocity (u) and the pressure (P) at different times from the initial time $t = 0$ to $t = 30$ s for the test case B1-Q90. Fig. 7 shows the distribution of porosity for the same test case at $t = 30$ s. During the first 8.0 seconds, flow depth decreases between the inflow boundary (X^{in}) and the end of the transition zone (X_2^{tr}) after which the porosity is fixed to the profile shown in Fig. 1. Then, flow develops in the constant-depth region until about $t = 20$ s when it becomes steady. For each test case, to achieve a constant depth between X_2^{tr} and X^{out}, different values of the outlet imaginary wall height H_{ow} are applied and the uniformity of the flow is checked. The optimum H_{ow} for all the test cases were found to be in the range of 90 to 100 % of the experimental total depth ($z_{ws} - z_b$).

A measuring zone is chosen from $X_l^s = X^{in} + 4.5H_t^{in}$ to $X_r^s = X^{in} + 6.5H_t^{in}$ with a mid-section at $X_m^s = X^{in} + 5.5H_t^{in}$ (Fig. 7). The distance between the end of the measuring section X_r^s to the outlet boundary line X^{out} is about $1.5H_t^{in}$. To post-process the simulation results, a fixed grid is defined over the measuring zone with grid spacing of 5 mm where particle quantities are averaged at grid points using the cubic Spline function (Monaghan and Lattanzio, 1985).

To check steadiness of the flow, water surface elevation and streamwise velocity at the mid-section X_m^s are compared at different times. When the changes in the water depth and depth-averaged streamwise velocity become less than 2%, flow is considered to be steady. After $t = 20$ s, the difference falls below 1% for all the eight test cases.

In order to check uniformity of the flow, streamwise velocity profiles at sections X_l^s, X_m^s and X_r^s are averaged over time, and then compared. When the difference between the depth-averaged value is less than 2%, flow is considered to be uniform over the measuring zone. The time averaging is performed over a period of 10 s during the steady state, from $t = 35$ s to 45 s. For most of the test cases, the difference is below 2%, while in few of them (at higher flow rates) it exceeds 2% slightly.

According to the above-mentioned criteria, the steadiness and uniformity of flow are satisfied for all the eight cases simulated in the present study. As an example, Fig. 8 presents the calculated velocity profiles at section X_m^s at different times (left) and the time-averaged profiles at sections X_l^s, X_m^s and X_r^s (right) for the test case B1-Q90. Besides, Fig. 9 presents the distribution of particles with their velocity and pressure at the steady state (t = 30 s) within the measuring section (between X_l^s and X_r^s) for the same test case. The figure also illustrates the change of particle's volume due to the change of porosity from one region to another, i.e. higher particle spacing in the regions with smaller porosity.

Looking at Figs. 5 and 6, noise is clearly seen within and just after the inflow transition zone as well as at the outlet boundary both in the streamwise velocity and pressure. A part of the noise in the inflow area is due to the condition of flow as a higher depth flow is transitioned into a lower depth within a relatively short distance. The other part of the noise is numerical, and due to the scheme used for pressure calculation, i.e. WCSPH. The noise in the outlet boundary is purely numerical, and a result of the instabilities due to the presence of an imaginary wall against flow. There is also some noise in the measuring section in the distribution of particles, particularly those near the free surface (Fig. 9). This noise is related to the inaccurate pressure estimation in the WCSPH scheme, especially that the estimated pressure is not exactly zero at the free surface boundary. Despite these errors, the estimated velocity and pressure are quite smooth within the measuring section, and therefore, uniform flow condition with the desirable results of velocity and shear stress (as presented in the next sections) is obtained.

5.2. Validity of the turbulence model

According to Pope (2000), for a reliable LES, more than 80% of the turbulent kinetic energy should be resolved. Considering the Kolmogorov spectra of turbulence, as depicted in Fig. 10 in the wavenumber (k) domain, a reliable LES-SPH model aims at resolving the turbulent energy (E) produced by large eddies (corresponding to ranges below the cut-off wavenumber π/Δ_m) and modelling the energy generated by smaller eddies (corresponding to wavenumbers above π/Δ_m).

However, this is not the case in the present macroscopic simulations since, even using the Smagorinsky model with a filter width (Δ_m) of about the particle spacing size and modelling the energy in the wavenumbers above π/Δ_m, still most of the energy in the larger eddies (wavenumbers below π/Δ_m) is not resolved by the computational resolution due to missing a large amount of eddies which, in the physical model, are generated as a result of flow blockage by the solid elements in the roughness layer. If Δ_r is a characteristic length scale of the missing roughness-related eddies, a macroscopic model resolves only the length scales larger than Δ_r (wavenumbers below π/Δ_r), which are in fact associated with the variations in the 'macroscopic velocity'. Therefore, the turbulent energy associated with the wavenumbers between π/Δ_r and π/Δ_m are missing in the macroscopic modelling of a rough bed. This was the reason for employing a mixing-length distribution for the eddy-viscosity coefficient in the present model, which is similar to the treatment in the Reynolds Averaged Navier-Stokes (RANS) models. As will be shown in the following sections, the application of the mixing-length profile introduced in Eq. (7) will recover the missing part of the turbulence effect and produce the required balance in the flow momentum.

Here, the test case B1-Q90 is simulated by using both the standard Smagorinsky model with the constant of $C_s = 0.15$ and the present three-layer mixing-length model. The resolved shear stress (τ_r) is computed as $\rho\langle\tilde{u}\tilde{w}\rangle$, where $\tilde{u}$ and $\tilde{w}$ are, respectively, the deviations of the SPH-estimated streamwise and vertical particle velocities from their spatial averages, and $\langle\rangle$ denotes the spatial average operator. The averaging is performed using the cubic Spline kernel function with a smoothing length of $1.2l_0$. Then, the total shear stress (τ_t) for each case is computed by adding the modelled shear stress (τ_s or τ_l, which are the shear stresses estimated by the Smagorinsky or the mixing-length models, respectively) to the resolved one.

Fig. 11 represents and compares the shear stress as well as the velocity profiles estimated by both models for the test case B1-Q90. It shows that the resolved shear stress is almost zero except in the roughness layer where the variations in the macroscopically averaged velocity are significant, and that almost all the turbulence effect needs to be modelled in the present problem. It also indicates that the Smagorinsky model is not suitable for such conditions, while the present mixing-length model performance is superior.

5.3. Velocity and shear stress profiles

In this section, the results of streamwise velocity and turbulent shear stress are presented for all the eight test cases. SPH-estimated velocity, its gradient, and shear stress are averaged over a time period of 10 s from $t = 35$ s to 45 s at the mid-section X_m^s of the measuring zone, and compared to the experimental profiles in Figs. 12 and 13 for the bed conditions B1 and B2, respectively.

In all cases, streamwise velocity is slightly underestimated by the model. The underestimation appears as a vertical shift in the velocity profiles of the test cases associated with bed B1, while it seems not constant through the depth for the test cases of bed B2, but it is higher around the roughness layer and lower near the water surface. In addition to the effect of the numerical noise discussed in Section 5.1, the underestimation of velocity could be due to an underestimation/overestimation of stress-strain components which may have been caused by an imprecise estimation of the coefficients in either the drag or turbulence closure models. The determination of those coefficients was based on physical knowledge and data in the free-flow region and upper part of the roughness layer where data is available, while the investigation of this issue was not possible for the flow regions within the porous layer due to the lack of knowledge and data. However, there is still good agreement between numerical and experimental profiles. This can be seen from Table 3 where the Root Mean Square Error (RMSE) of the numerical profiles of velocity and its gradient with respect to the experimental data are presented for both in the roughness and free-flow layers. For this calculation, the experimental gradients are firstly smoothed by applying a moving average procedure over three adjacent points. According to Aberle (2006), smoothing the gradients is necessary due to the ill-posed nature of estimating velocity derivatives from point velocity measurements that contain a small but finite experimental measurement uncertainty. The velocity gradients below the centre of the roughness layer z_a $(= z_t + \Delta_s/2)$ are not considered due to their large scatter even after smoothing. These non-physical scatters can be attributed to the more limited number of measuring points in the lower part of the roughness layer due to the existence of solid material, as well as the above-mentioned ill-posed problem.

As mentioned, due to the lack of knowledge and data of the flow and bed conditions within the porous sediment layer, the determination of the drag coefficients in this layer is difficult. Although these coefficients have been chosen based on established empirical relationships, they could still be imprecise due to the fact that the flow and bed conditions in the present study are slightly different from those used for deriving the empirical equations (here, the Ergun's equation). It is never possible to determine the coefficients exactly, especially for the present natural bed conditions. However, here, we try to tune the drag coefficient in the porous sediment layer (i.e., c_2 in Eq. (6)) numerically, to obtain a better match with the experimental profiles. Using the value of $c_2 = 1.20$ for the test cases B1-Q90, B1-Q150, B2-Q90 and B2-Q150, the velocity profiles are obtained as presented in Fig. 14 in comparison with the experimental data. The good match here indicates that in the results presented in Figs. 12 and 13, the amount of drag from the porous bed material was probably overestimated by using the original Ergun's constants. The value used here is about 30 % lower than that originally proposed by Ergun ($c_2 = 1.75$). It is noted that, Ergun (1952) suggested the value of $c_2 = 1.75$ (together with $c_1 = 150$) based on fitting his relationship to a number of data sets, where although the fitting curve showed a good match with the data, there were still some scatters. In other words, the Ergun's fit represents an average of a set of different conditions which could deviate quite significantly from reality in the case of natural beds. However, the idea behind using the Ergun's original constants for the present simulations was that it is reasonable to tolerate the expected error, if it is within an acceptable range (Table 3), rather than constructing the model based on arbitrary numerical adjustments.

5.4. Convergence and error analysis

In order to investigate the convergence of the numerical solution, a sensitivity analysis of the computational resolution is performed for the test case B1-Q90. The simulation of the test case is repeated with several particle spacing values (l_0 = 9, 7, 5 and 3 mm) and then, following Wang et al. (2019), mean relative error between numerical and experimental profiles is calculated for each one. The calculation of the error is performed for both velocity and its gradient. For this, Spline curves are firstly fitted to the velocity profiles and their gradients; and then, the error is computed. Fig. 15 shows the fitted curves to the velocity profiles (left) and their gradients (right); and Fig. 16 presents the relationship between the initial particle spacing (l_0) and the mean relative error (Er) of these profiles, where the slope of the lines fitted to the points represent the convergence rate of the numerical solution, which is near 0.9 for both the streamwise velocity and its gradient, meaning that the convergence rate is nearly linear in this study.

5.5. Analysis of velocity profiles

Through the double-averaging procedure of Nikora et al. (2007a), Koll (2006) suggested the following equation for the velocity distribution in the logarithmic layer above a rough bed.

$$\frac{u}{u_*} = \frac{1}{\kappa} \ln \frac{z - z_d}{z_R - z_d} + \frac{u_R}{u_*} \tag{9}$$

where u_* is the shear velocity; κ is the von-Karman constant (= 0.41); z and u are, respectively, the vertical position and the double-averaged velocity at that position; z_R is the geodetic height of the roughness layer which is closely related to the roughness crest z_c (Aberle, 2006); u_R is the double-averaged velocity at z_R; and z_d is the zero-plane displacement.

As mentioned in Section 5.3, the SPH-estimated velocity is averaged over a period of 10 s; therefore, it is equivalent to the double-averaged velocity in Eq. (9). Here, replacing z_R and u_R with, respectively, z_c and u_c (which denote the velocity at z_c) in Eq. (9), the curve obtained by this equation is fitted to both the experimental and calculated velocity profiles for all the eight independent test cases; and through this process, the zero-plane displacement z_d is obtained. For each profile, z_d is initially set to z_t (roughness trough) and then increased by increment of 1 mm and the coefficient of determination (R^2) is calculated. The value of z_d that provides the highest R^2 is selected as the zero-plane displacement of that profile. The estimated z_d and the corresponding R^2 values are represented in Table 4; and the velocity profiles fitted to Eq. (9) are shown in Figs. 17 and 18 for the experimental and numerical data, respectively. Note that in the derivation of Eq. (9), a linear mixing-length, i.e. $l_m = \kappa (z - z_d)$, was adopted; while in the present SPH model, l_m is estimated by the non-linear relationship in Eq. (7). Besides, the higher zero-plane displacement of the SPH profiles explains the small vertical shift in Figs. 12 and 13.

For the velocity in the roughness layer, Nikora et al. (2004) suggested three possible distributions, i.e. constant, linear and exponential, depending on the roughness geometry, flow conditions, and relative submergence. The constant velocity was suggested for cases such as partially submerged vegetation in streams where the vertical variations of total fluid stress or roughness geometry function (equivalent to porosity ϕ in this study) in the roughness layer are approximately zero; exponential distribution was proposed for flow through well-submerged roughness elements with $d\phi/dz \approx 0$ and with the overlying layer being the dominant source of momentum, such as a low-slope flow over aquatic plants; and finally, the linear distribution was suggested for gravel beds where the roughness density function monotonically decreases from one at the level of the roughness crest to zero or its minimum value at the level of the roughness trough for impermeable and permeable beds, respectively.

The conclusion of linearity of the velocity profile in the roughness layer in Nikora et al. (2004) (as also shown in Koll, 2006) was drawn for rough beds made of a small number of layers of quite closely packed elements of quite constant height, where the spacing of the elements was almost constant. In the derivation of the linear model, Nikora et al. (2004) assumed that the product $\phi[(f_p + f_v) - \rho g S_0]$ is approximately constant in the roughness layer. f_p and f_v denote the form and viscous drag terms in their double-averaged momentum equation. Assuming f_v is much smaller than f_p in the roughness layer in the present flow conditions, and considering that f_p is equivalent to $\rho\mathbf{A}$ in the present SPHAM equation of momentum (Eq. (2)), $\phi[\rho A_x - \rho g S_0]$ (A_x being the streamwise component of $\mathbf{A}$) of the numerical data is computed and presented in Fig. 19. As can be seen, the vertical distribution of $\phi[\rho A_x - \rho g S_0]$ is not constant for the present test cases. This is related to the vertically non-uniform spatial distribution of the bed surface, where sediments are neither closely packed nor with constant spacing and height. Therefore, although the linear model has worked well for various conditions so far, here, we investigate an alternative distribution of velocity in the roughness layer for the present bed conditions as follows.

According to our observations, an S-shaped distribution with continuously changing gradient may provide a better representation of the present velocity profiles in the roughness layer. S-shaped velocity distribution has previously been reported in a number of studies for rough-bed flows (Ferro and Baiamonte, 1994; Katul, 2002; Zeng and Li, 2012). Although those studies have investigated the S-shape velocity distribution in a layer including the roughness layer and its overlaying flow with quite low relative submergence, the same mechanism may exist within the roughness layer of the present test cases, i.e. an inflectional profile creates a smooth transition from the low constant velocity in the porous layer (below z_t) to the faster flow in the free-flow region (above z_c).

To investigate this issue, here, we consider a sigmoid function, as in Eq. (10), to represent the velocity distribution in the roughness layer. Looking at the velocity gradients in the roughness layer shown in Fig. 20, the bell-shaped profiles, although non-symmetric, imply that a sigmoid function may better represent the velocity compared to a linear function (since the first derivative of a sigmoid is bell-shaped while the gradient of a linear velocity is constant). Making use of the fact that flow regime in shallow rough-bed flows is analogous to turbulent flows within and above vegetation canopies, Katul (2002) used a function similar to Eq. (10) for velocity distribution within and above the roughness layer with an inflection point near the mean height of the roughness elements (close to z_c in the present study). However, here, the inflection of the sigmoid curve is assumed to be at the centre of the roughness layer z_a due to the fact that the peak of the numerical velocity gradients occurs at z_a in almost all the present test cases (Fig. 20). A possible reason for a lower inflection point in the present data compared to other reported data in the literature may be related to the condition of the bed (vertical variation in porosity) and the spatial resolution and density of the velocity measurements. In the present physical model, the larger roughness elements on the bed surface were not placed in a packed style, but with considerable spacing between them. This could have led the inflection point to move lower within the roughness layer, probably around z_a.

$$Y = \frac{\alpha}{1 + e^{-\beta X}} \tag{10}$$

where $Y = u/u_*$, $X = (z - z_a)/\Delta_s$, and α and β are constants. This function is first used to fit curves to the experimental velocity profiles in the upper part of the roughness layer, i.e. $z_a \leq z \leq z_c$. The result is shown in Fig. 21. As a second trial, the derivative of Eq. (10) with respect to z, i.e. $dY/dz = ab\,e^{-bX}/(1+e^{-bX})^2$ is applied to fit curves to the experimental velocity gradients, as depicted in Fig. 22. The sigmoid function seems to provide a reasonable fit to the data. However, unfortunately, such high resolution data is not available in the lower part of the roughness layer, or there are only a few data points available below z_a with a large scatter in the data especially in the velocity gradients. Therefore, it is not possible to rigorously validate the sigmoid distribution of the data in the lower part.

However, the SPH velocity profiles are available over the entire depth, thus they are tested with the sigmoid function and the result is presented in Fig. 23. The SPH profiles in the lower part ($z_t \leq z \leq z_a$) present better match with the sigmoid function than in the upper part ($z_a < z \leq z_c$). This is shown in Table 5 where the R^2 values calculated for the lower and upper parts are presented. A possible reason is that the curvature in the lower part is a result of a smooth transition from a constant value (in the bed), while the upper bound at z_c reaches a logarithmic distribution. However, in a sigmoid curve, both the lower and upper bounds end with constant values. In other words, the sigmoid curve and its gradient are symmetric with respect to z_a, but the present velocity profiles and their gradients are to some extent non-symmetric due to different flow characteristics at the lower and upper bounds. The deviation of the velocities from the sigmoid function is more clearly seen in Fig. 24 where the gradients of the sigmoid curves in Fig. 23 are compared with the SPH velocity gradients.

It is noted that, assuming the central part of a sigmoid curve can be to some extent considered as a linear-like profile, the extent of this linear part is larger in the test cases associated with bed B2, probably due to the larger thickness of the roughness layer. In such a case, X in Eq. (10) can be replaced with higher order terms, for example, $X + X^3$ to cancel the third degree derivatives and create a longer linear part in the fitted sigmoid curves. Another approach would be investigating smooth transitions from a linear to a logarithmic distribution in the upper bound and from the same linear distribution to a constant in the lower bound of the roughness layer. Further investigation of this issue is beyond the scope of the present work and is considered as a future study.

6. Conclusions

With improvements in the turbulence modelling, inflow/outflow boundaries, and treatment of the rough interface boundary, a WCSPH model was developed for simulating momentum transfer mechanisms in turbulent open channel flows over and within natural porous beds. Ergun's equation with its original drag coefficients was employed to simulate the frictional effects of the solid skeleton within the lower sediment layer while the drag effect within the roughness layer was incorporated by a modified version of the drag force model proposed by Kazemi et al. (2017). It was shown that the standard Smagorinsky model is not sufficient to model turbulence induced shearing effects in the macroscopic simulation of rough boundaries, especially within the roughness layer; and therefore, a generalised three-layer mixing-length model which represents the different sizes of eddy flow structures expected in the free-flow region, roughness layer and porous bed, was proposed. Besides, a porous inflow boundary as well as an imaginary outlet wall were introduced to obtain uniform flow conditions.

Eight test cases of turbulent flows over two porous beds were simulated (with the calibration of the proposed generalised mixing-length model for each bed condition), and the results of velocity and turbulent shear stress were compared with the experimental data. The simulated flow conditions cover a wide range of typical conditions that one would see in water worked gravel bed rivers. The proposed inflow/outflow boundary techniques were capable of generating steady uniform flows within a short computational domain, and the drag and turbulence models produced the required momentum balance between the porous and free-flow regions, so that a good agreement with the detailed experimental velocity data was achieved for various bed and flow conditions. The application of the proposed three-layer mixing-length model, which adopts a nonlinear distribution in the free-flow layer with its extension into the roughness layer based on the physical conditions of bed and flow, was crucial for the superior performance of the model.

Through a detailed velocity analysis, it was found that an S-shape curve, in which the variation in the gradient is smooth and has no discontinuities unlike the linear model, better represents the vertical velocity profile within the roughness layer of gravel beds such as the ones simulated in the present study. Here, the bed surface demonstrates a non-uniform condition with larger roughness elements not being placed in a packed style, but with more open spacing between them. The S-shape profile reflects the effect of the non-uniform variation in porosity as it simulates the impact on the fluid drag caused by the spatial organisation of the sediment particles. Besides, it was observed that the change of gradient is more substantial in the lower part of the roughness layer, where the velocity is connected to a constant distribution in the sediment bed; while in the upper part, a less rapid transition to the overlying logarithmic layer is present.

In spite of the limitations with regard to the macroscopic modelling of the porous media and the determination of the coefficients of the closure models, the present study showed that the SPH method has the capacity of simulating complex turbulent channel flows over natural gravel beds with highly sheared interfacial boundaries. The potential future improvements of the present model, particularly with regard to the numerical noise discussed in Section 5.1, would include utilisation of more advanced numerical schemes such as the Incompressible SPH higher-order pressure solution scheme (e.g. Gotoh et al., 2014) and the Optimised PS technique (e.g. Khayyer et al., 2017a) in order to enhance the stability and accuracy of the solution.

Acknowledgement

This work was supported by the Research Executive Agency, through the 7th Framework Programme of the European Union, Support for Training and Career Development of Researchers (MarieCurie-FP7-PEOPLE-2012-ITN), which funded the Initial Training Network (ITN) HYTECH 'Hydrodynamic Transport in Ecologically Critical Heterogeneous Interfaces', No. 316546.

References

Aberle, J., 2006. Spatially averaged near-bed flow field over rough armor layers, in: Int. Conf. on Fluvial Hydraulics River Flow 2006, Lisbon, Portugal, p. 153–162.

Aberle, J., 2007. Measurements of armour layer roughness geometry function and porosity. Acta Geophysica 55, 23–32.

Aberle, J., Koll, K., Dittrich, A., 2008. Form induced stresses over rough gravel-beds. Acta Geophysica 56, 584–600.

Akbari, H., 2014. Modified moving particle method for modeling wave interaction with multi layered porous structures. Coastal Engineering 89, 1-19.

Akbari, H., Namin, M., 2013. Moving particle method for modeling wave interaction with porous structures. Coastal Engineering 74, 59-73.

Antuono, M., Marrone, S., Colagrossi, A., Bouscasse, B., 2015. Energy balance in the δ-SPH scheme. Computer Methods in Applied Mechanics and Engineering 289, 209–226.

Aristodemo, F., Marrone, S., Federico, I., 2015. SPH modeling of plane jets into water bodies through an inflow/outflow algorithm. Ocean Engineering 105, 160-175.

Breugem, W., Boersma, B., 2005. Direct numerical simulations of turbulent flow over a permeable wall using a direct and a continuum approach. Physics of Fluids 17, 025103.

Breugem, W., Boersma, B., Uittenbogaard, R., 2006. The influence of wall permeability on turbulent channel flow. Journal of Fluid Mechanics 562, 35–72.

Dalrymple, R., Knio, O., 2001. SPH modelling of water waves, in: Proceedings of the Coastal Dynamics, Lund, Sweden. pp. 11–15.

Di Mascio, A., Antuono, M., Colagrossi, A., Marrone, S., 2017. Smoothed particle hydrodynamics method from a large eddy simulation perspective. Physics of Fluids 29, 035102.

Ergun, S., 1952. Fluid flow through packed columns. Chemical Engineering Progress 48, 89-94.

Fang, H., Han, G., He, X., Dey, S., 2018. Influence of permeable beds on hydraulically macro-rough flow. Journal of Fluid Mechanics 847, 552–590.

Federico, I., Marrone, S., Colagrossi, A., Aristodemo, F., Antuono, M., 2012. Simulating 2D open-channel flows through an SPH model. European Journal of Mechanics-B/Fluids 34, 35-46.

Ferro, V., Baiamonte, G., 1994. Flow velocity profiles in gravel-bed rivers. Journal of Hydraulic Engineering 120, 60–80.

Ghaitanellis, A., Violeau, D., Ferrand, M., El Kadi Abderrezzak, K., Leroy, A., Joly, A., 2018. A SPH elastic-viscoplastic model for granular flows and bed-load transport. Advances in Water Resources 111, 156–173.

Gotoh, H., Khayyer, A., 2018. On the state-of-the-art of particle methods for coastal and ocean engineering. Coastal Engineering Journal 60, 79–103.

Gotoh, H., Khayyer, A., Ikari, H., Arikawa, T., Shimosako, K., 2014. On enhancement of Incompressible SPH method for simulation of violent sloshing flows. Applied Ocean Research 46, 104–115.

Gotoh, H., Shibahara, T., Sakai, T., 2001. Sub-particle-scale turbulence model for the MPS method – Lagrangian flow model for hydraulic engineering. Computational Fluid Dynamics Journal 9, 339–347.

Gui, Q., Dong, P., Shao, S., Chen, Y., 2015. Incompressible SPH simulation of wave interaction with porous structure. Ocean Engineering 110, Part A, 126-139.

Hahn, S., Je, J., Choi, H., 2002. Direct numerical simulation of turbulent channel flow with permeable walls. Journal of Fluid Mechanics 450, 259-285.

Harada, E., Ikari, H., Shimizu, Y., Khayyer, A., 2018. Numerical investigation of the morphological dynamics of a step-and-pool riverbed using DEM-MPS. Journal of Hydraulic Engineering 144, 04017058.

Hu, F., Wang, Z., Tamai, T., Koshizuka, S., 2019. Consistent inlet and outlet boundary conditions for particle methods. International Journal for Numerical Methods in Fluids , 1–19.

Katul, G., 2002. A mixing layer theory for flow resistance in shallow streams. Water Resources Research 38, 1250.

Kazemi, E., Nichols, A., Tait, S., Shao, S., 2017. SPH modelling of depth-limited turbulent open channel flows over rough boundaries. International Journal for Numerical Methods in Fluids 83, 3–27.

Kazemi, E., Tait, S., Shao, S., 2019. SPH based numerical treatment of the interfacial interaction of flow with porous media. International Journal for Numerical Methods in Fluids , 1–27doi:10.1002/fld.4781.

Khayyer, A., Gotoh, H., 2010. On particle-based simulation of a dam break over a wet bed. Journal of Hydraulic Research 48, 238–249.

Khayyer, A., Gotoh, H., Shao, S., 2008. Corrected incompressible SPH method for accurate water-surface tracking in breaking waves. Coastal Engineering 55, 236–250.

Khayyer, A., Gotoh, H., Shimizu, Y., 2017a. Comparative study on accuracy and conservation properties of two particle regularization schemes and proposal of an optimized particle shifting scheme in ISPH context. Journal of Computational Physics 332, 236–256.

Khayyer, A., Gotoh, H., Shimizu, Y., Gotoh, K., 2017b. On enhancement of energy conservation properties of projection-based particle methods. European Journal of Mechanics - B/Fluids 66, 20–37.

Khayyer, A., Gotoh, H., Shimizu, Y., Gotoh, K., Falahaty, H., Shao, S., 2018. Development of a projection-based SPH method for numerical wave flume with porous media of variable porosity. Coastal Engineering

140, 1–22.

Koll, K., 2006. Parameterisation of the vertical velocity profile in the wall region over rough surfaces, in: Int. Conf. on Fluvial Hydraulics River Flow 2006, Lisbon, Portugal, p. 163–171.

Leonardi, A., Pokrajac, D., Roman, F., Zanello, F., Armenio, V., 2018. Surface and subsurface contributions to the build-up of forces on bed particles. Journal of Fluid Mechanics 851, 558–572.

Leroy, A., Violeau, D., Ferrand, M., Kassiotis, C., 2014. Unified semi-analytical wall boundary conditions applied to 2-D incompressible SPH. Journal of Computational Physics 261, 106–129.

Lian, Y., Dallmann, J., Sonin, B., Roche, K., Liu, W., Packman, A., Wagner, G., 2019. Large eddy simulation of turbulent flow over and through a rough permeable bed. Computers and Fluids 180, 128–138.

Meringolo, D., Liu, Y., Wang, X.Y., Colagrossi, A., 2018. Energy balance during generation, propagation and absorption of gravity waves through the δ-LES-SPH model. Coastal Engineering 140, 355–370.

Monaghan, J., Lattanzio, J., 1985. A refined particle method for astrophysical problems. Astronomy & Astrophysics 149, 135–143.

Nezu, I., Rodi, W., 1986. Open-channel flow measurements with a laser doppler anemometer. Journal of Hydraulic Engineering 112, 335–355.

Nikora, V., Koll, K., McEwan, I., McLean, S., Dittrich, A., 2004. Velocity distribution in the roughness layer of rough-bed flows. Journal of Hydraulic Engineering 130, 1036–1042.

Nikora, V., McEwan, I., McLean, S., Coleman, S., Pokrajac, D., Walters, R., 2007a. Double-averaging concept for rough-bed open-channel and overland flows: theoretical background. Journal of Hydraulic Engineering 133, 873–883.

Nikora, V., McLean, S., Coleman, S., Pokrajac, D., McEwan, I., Campbell, L., Aberle, J., Clunie, D., Koll, K., 2007b. Double-averaging concept for rough-bed open-channel and overland flows: applications. Journal of Hydraulic Engineering 133, 884–895.

Pahar, G., Dhar, A., 2016. Modeling free-surface flow in porous media with modified incompressible SPH. Engineering Analysis with Boundary Elements 68, 75-85.

Pahar, G., Dhar, A., 2017. On modification of pressure gradient operator in integrated ISPH for multifluid and porous media flow with free-surface. Engineering Analysis with Boundary Elements 80, 38–48.

Pope, S., 2000. Turbulent Flows. Cambridge, UK: Cambridge University Press.

Ren, B., Wen, H., Dong, P., Wang, Y., 2014. Numerical simulation of wave interaction with porous structures using an improved smoothed particle hydrodynamic method. Coastal Engineering 88, 88-100.

Ren, B., Wen, H., Dong, P., Wang, Y., 2016. Improved SPH simulation of wave motions and turbulent flows through porous media. Coastal Engineering 107, 14-27.

Rosti, M., Cortelezzi, L., Quadrio, M., 2015. Direct numerical simulation of turbulent channel flow over porous walls. Journal of Fluid Mechanics 784, 396–442.

Schmeeckle, M., Nelson, J., Shreve, R., 2007. Forces on stationary particles in near-bed turbulent flows. Journal of Geophysical Research 112:F02003.

Shakibaeinia, A., Jin, Y., 2010. A weakly compressible MPS method for modeling of open-boundary free-surface flow. International Journal for Numerical Methods in Fluids 63, 1208–1232.

Shao, S., 2010. Incompressible SPH flow model for wave interactions with porous media. Coastal Engineering 57, 304-316.

Shao, S., Lo, E., 2003. Incompressible SPH method for simulating Newtonian and non-Newtonian flows with a free surface. Advances in Water Resources 26, 787–800.

Stoesser, T., Frohlich, J., Rodi, W., 2007. Turbulent open-channel flow over a permeable bed, in: 32^{nd} IAHR Congress, International Association for Hydro-Environment Engineering and Research, Venice, Italy.

Wang, L., Khayyer, A., Gotoh, H., Jiang, Q., Zhang, C., 2019. Enhancement of pressure calculation in projection-based particle methods by incorporation of background mesh scheme. Applied Ocean Research 86, 320–339.

Zeng, C., Li, C., 2012. Modeling flows over gravel beds by a drag force method and a modified S–A turbulence closure. Advances in Water Resources 46, 84–95.

Table 1
The bed and flow conditions simulated in the present study.

Bed ID (armouring discharge)	z_t (mm)	z_c (mm)	Δ_s (mm)	Measuring discharge Q (l/s)	z_{ws} (mm)	H_c (mm)	Test ID
B1 (Q_{armour} = 180 l/s)	36.6	87.6	51	90	217	129	B1-Q90
				120	248	160	B1-Q120
				150	271	184	B1-Q150
				180	296	208	B1-Q180
B2 (Q_{armour} = 250 l/s)	-5.5	71.5	77	90	200	128	B2-Q90
				150	256	185	B2-Q150
				220	306	235	B2-Q220
				250	330	258	B2-Q250

Table 2
Mixing-length parameters adopted in the present simulations.

Bed	Test cases	l_{mb} (mm)	Δz_0 (mm)	κ_r	κ_f
B1	B1-Q90, B1-Q120, B1-Q150, B1-Q180	2	20	0.27	0.22
B2	B2-Q90, B2-Q150, B2-Q220, B2-Q250	2	0	0.15	0.22

Table 3
RMSE of the estimated velocity and its gradient with respect to the experimental data in the roughness layer as well as the free-flow region.

Tests	RMSE in the roughness layer ($z_a \leq z \leq z_c$)		RMSE in the free flow region ($z > z_c$)	
	u (m/s)	$\frac{\partial u}{\partial z}$ (1/s)	u (m/s)	$\frac{\partial u}{\partial z}$ (1/s)
B1-Q90	0.106	1.49	0.058	1.09
B1-Q120	0.115	2.22	0.066	0.98
B1-Q150	0.113	2.51	0.074	0.82
B1-Q180	0.118	2.31	0.072	0.98
B2-Q90	0.062	2.11	0.025	0.48
B2-Q150	0.119	1.78	0.041	1.07
B2-Q220	0.150	2.97	0.056	1.13
B2-Q250	0.176	3.28	0.057	1.52

Table 4
Zero-plane displacement based on fitting logarithmic curves to the velocity profiles in the free-flow region ($z > z_c$).

Tests	Experiment		SPH	
	$(z_d - z_t)/\Delta_s$	R^2	$(z_d - z_t)/\Delta_s$	R^2
B1-Q90	0.44	0.997	0.68	0.983
B1-Q120	0.45	0.998	0.65	0.985
B1-Q150	0.47	0.995	0.63	0.985
B1-Q180	0.47	0.989	0.63	0.988
B2-Q90	0.56	0.997	0.63	0.999
B2-Q150	0.48	0.991	0.69	0.996
B2-Q220	0.54	0.987	0.72	0.993
B2-Q250	0.52	0.976	0.76	0.984

Table 5
R^2 of the lower and upper parts of the SPH velocity profiles in the roughness layer fitted with the sigmoid function (Fig. 23).

Test cases	Lower part $z_t \leq z \leq z_a$	Upper part $z_a < z \leq z_c$
B1-Q90	0.985	0.926
B1-Q120	0.983	0.923
B1-Q150	0.994	0.972
B1-Q180	0.996	0.987
B2-Q90	0.994	0.958
B2-Q150	0.987	0.953
B2-Q220	0.990	0.950
B2-Q250	0.989	0.951

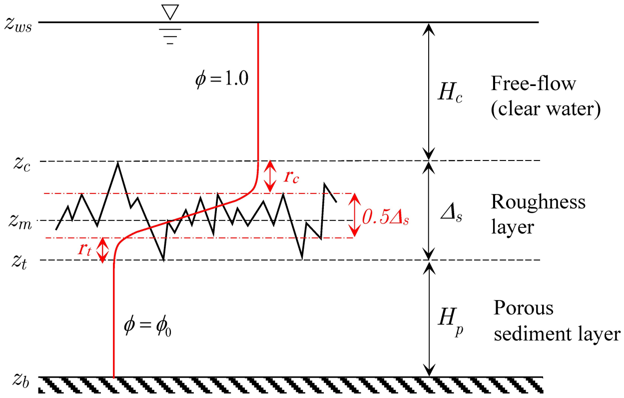

Fig. 1. Schematic 2D view of the bed condition and distribution of porosity over the total depth including porous bed, roughness layer and free-flow region.

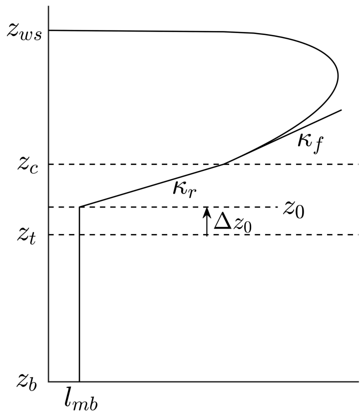

Fig. 2. Typical mixing-length distribution adopted in the present study.

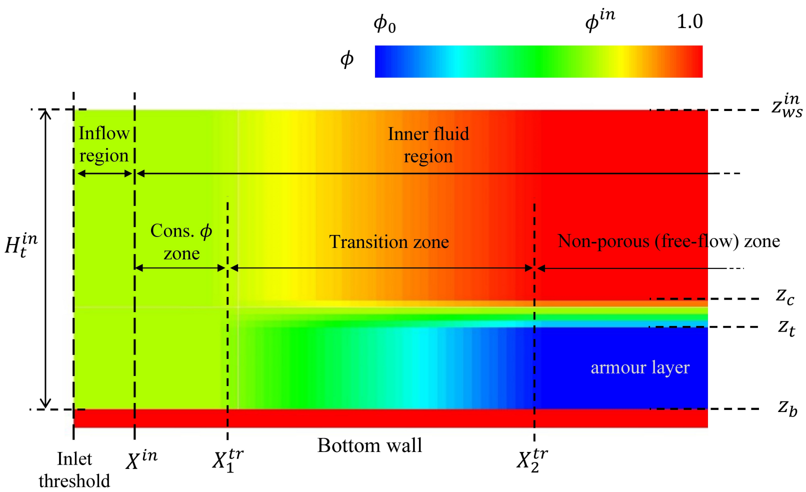

Fig. 3. Inflow boundary setup.

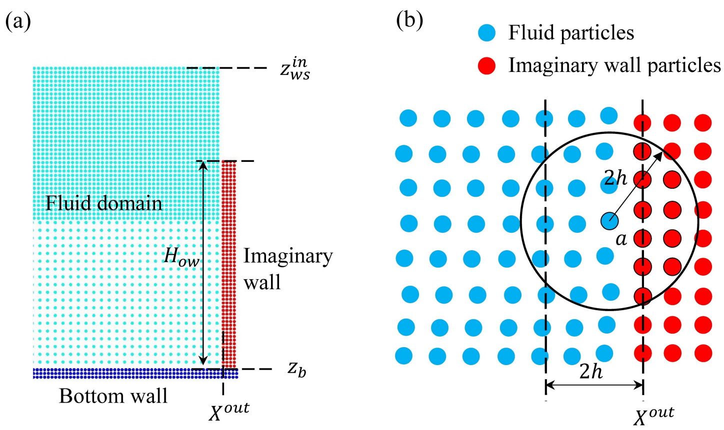

Fig. 4. Outflow boundary treatment: (a) initial set-up of the outflow boundary with an imaginary wall; (b) interaction between fluid and imaginary particles.

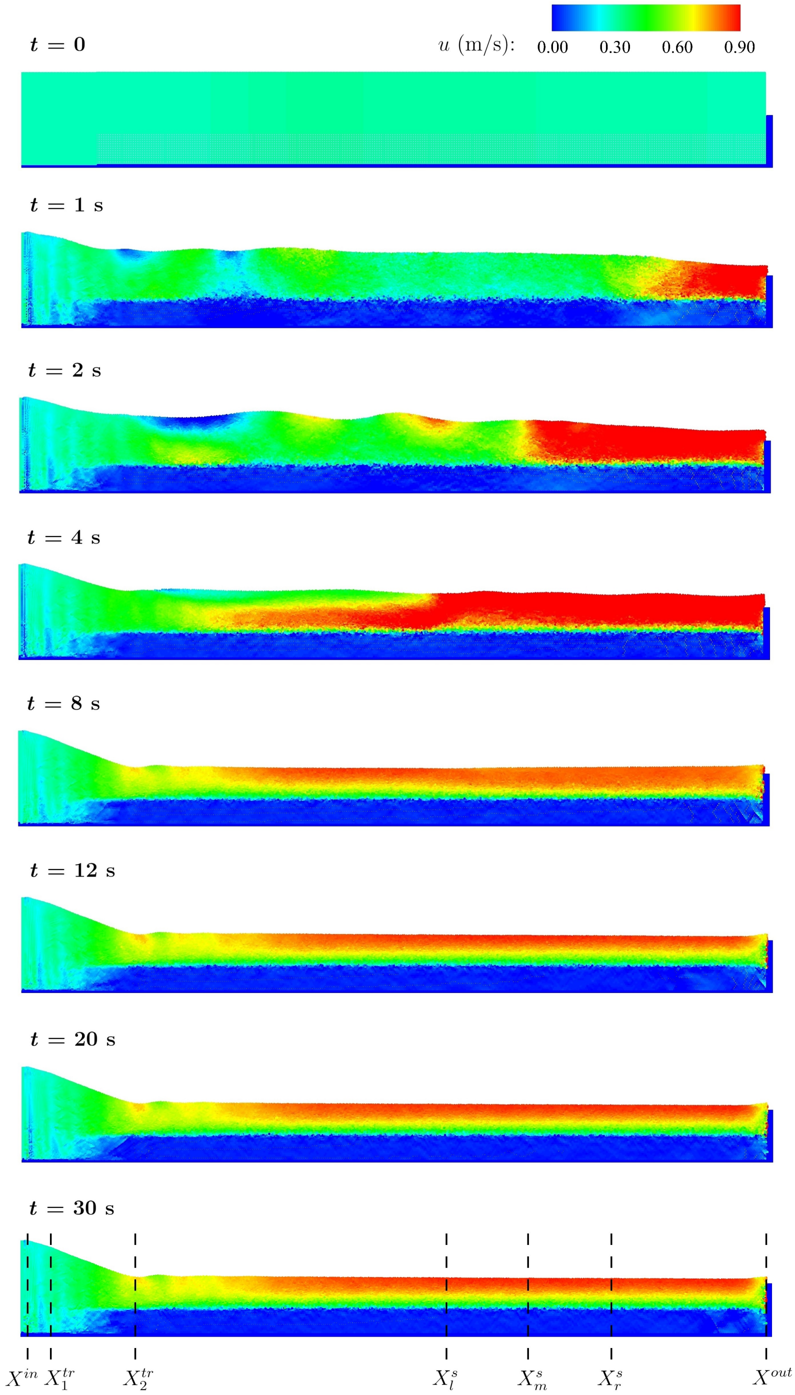

Fig. 5. Development of flow in test case B1-Q90: snapshots of particle position and velocity at different times from $t = 0$ to 30 s.

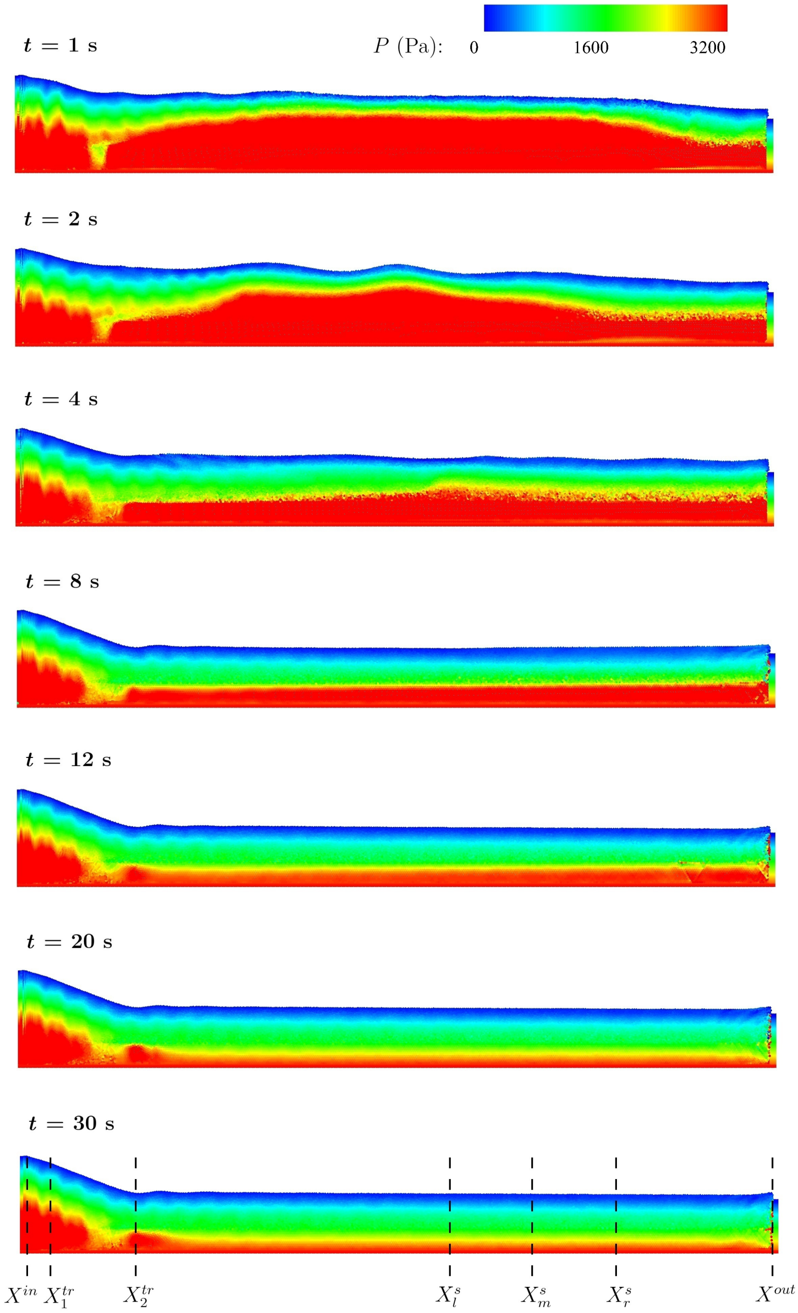

Fig. 6. Development of flow in test case B1-Q90: snapshots of particle position and pressure at different times from $t = 0$ to 30 s.

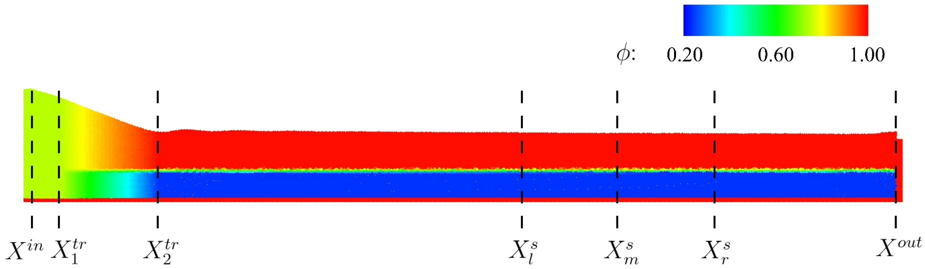

Fig. 7. Porosity distribution for test case B1-Q90 (t = 30 s).

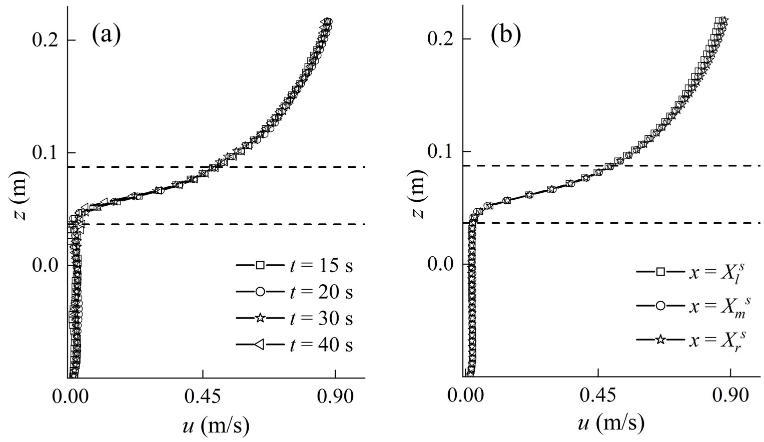

Fig. 8. Flow steadiness and uniformity for test case B1-Q90: (a) streamwise velocity distribution at section X_m^s at different times; and (b) streamwise velocity distribution at sections X_l^s, X_m^s and X_r^s averaged over a time period of 10 s. Dashed lines represent the bounds of the roughness layer (i.e. z_t and z_c).

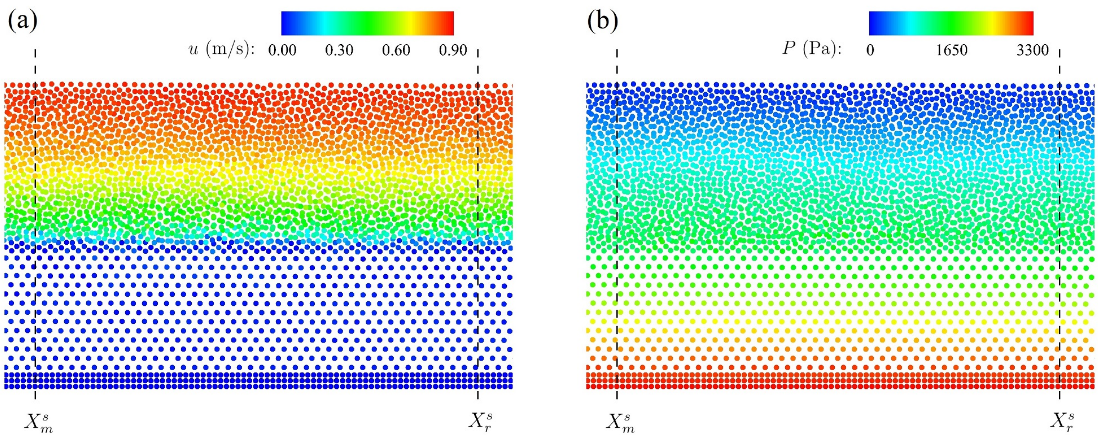

Fig. 9. Snapshots of particle position with (a) streamwise velocity, and (b) pressure for test case B1-Q90 within the measuring section in the steady state (t = 30 s).

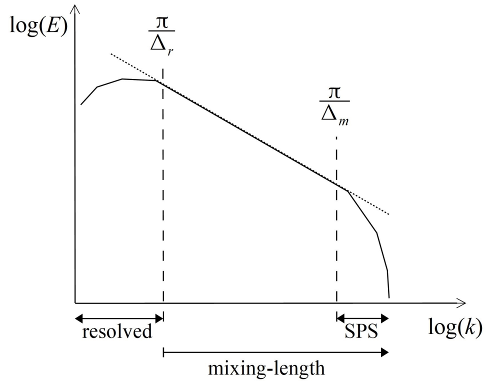

Fig. 10. Turbulence energy spectra and the resolved/modelled parts of the turbulence effect.

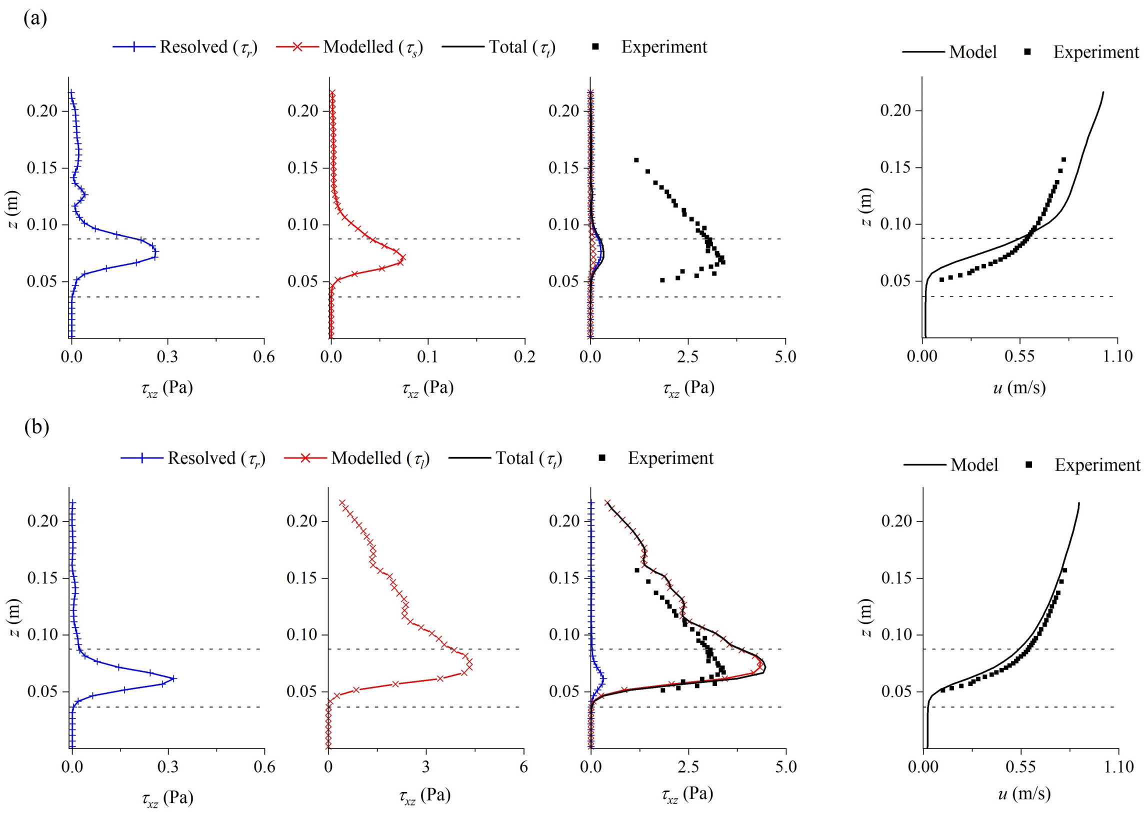

Fig. 11. Comparison of the performance of the model when using (a) the standard Smagorinsky model, and (b) the present mixing-length model, in the simulation of the test case B1-Q90.

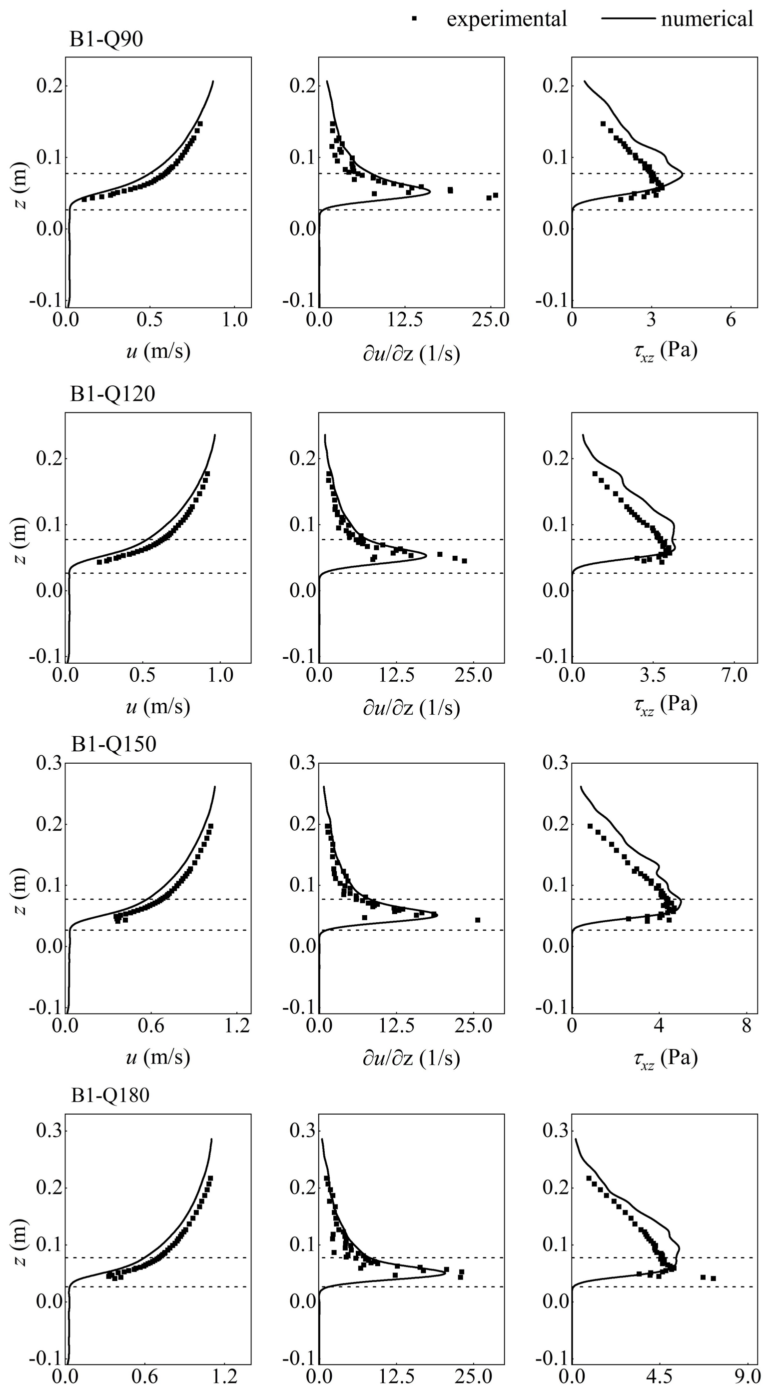

Fig. 12. Numerical results (solid lines) of streamwise velocity (left), its gradient (middle), and turbulent shear stress (right) in comparison with the experimental data (dark symbols) for the test cases associated with bed B1. Dashed lines show the bounds of the roughness layer (z_t and z_c).

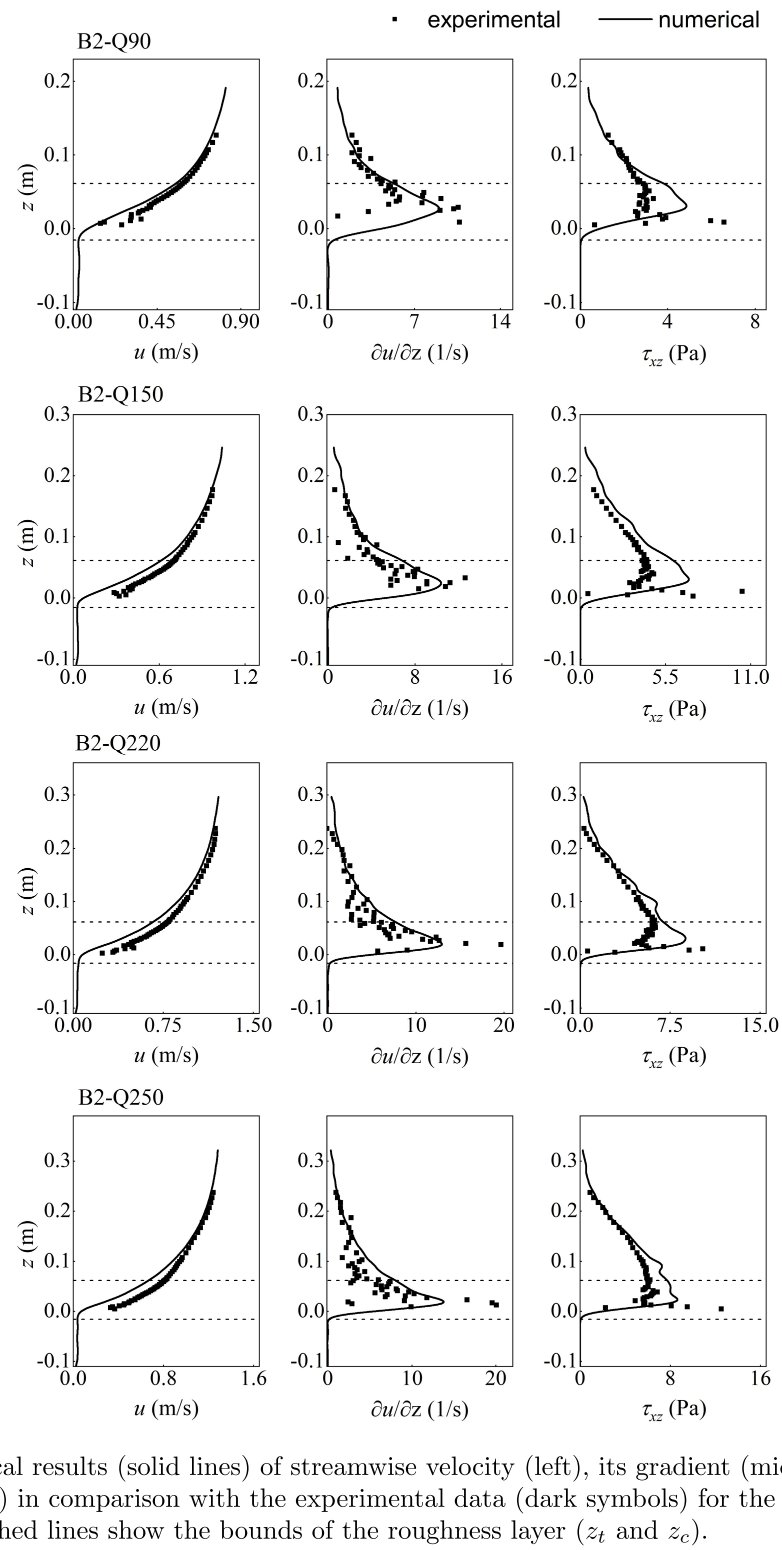

Fig. 13. Numerical results (solid lines) of streamwise velocity (left), its gradient (middle), and turbulent shear stress (right) in comparison with the experimental data (dark symbols) for the test cases associated with bed B2. Dashed lines show the bounds of the roughness layer (z_t and z_c).

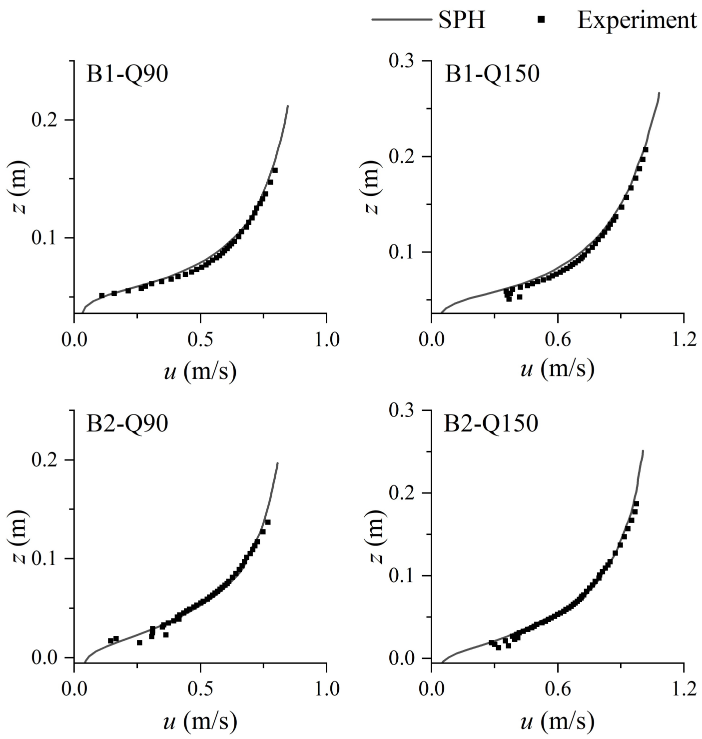

Fig. 14. Streamwise velocity profiles with using a lower drag coefficient (c_2) in the porous sediment layer.

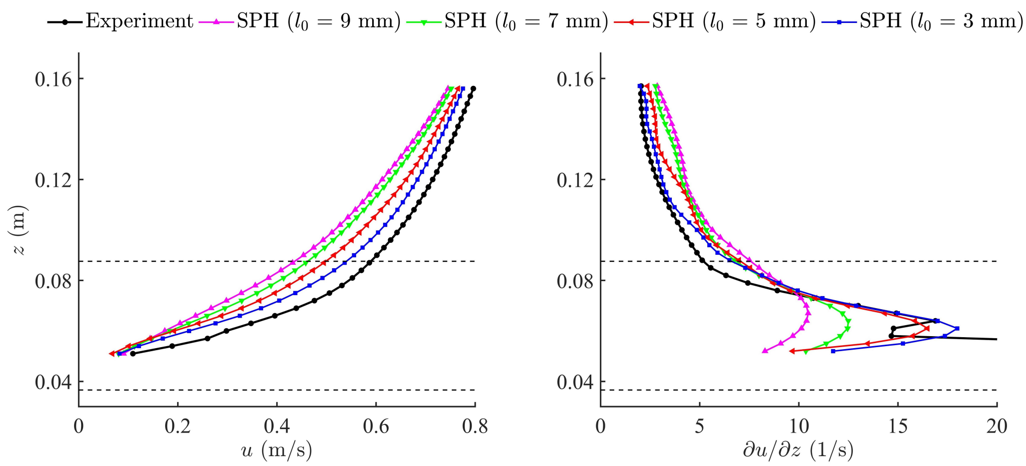

Fig. 15. Streamwise velocity profiles (left) and their gradients (right) estimated by the model with using different particle spacings.

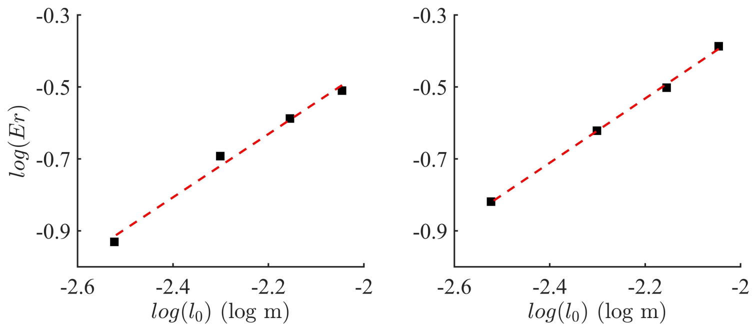

Fig. 16. Convergence and mean relative error analysis of the calculated streamwise velocity (left) and its gradient (right).

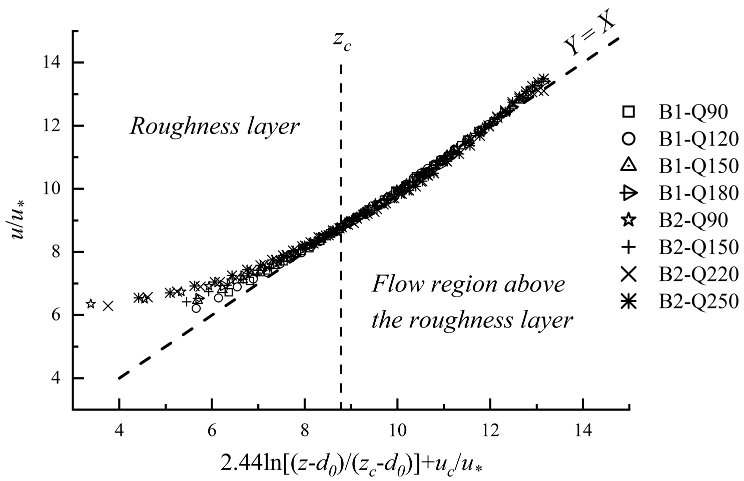

Fig. 17. Experimental streamwise velocity profiles with logarithmic distribution above the roughness layer. The location of z_c is different for different test cases in the present plot scale, however its average is indicated by a vertical dashed-line to show its approximate position.

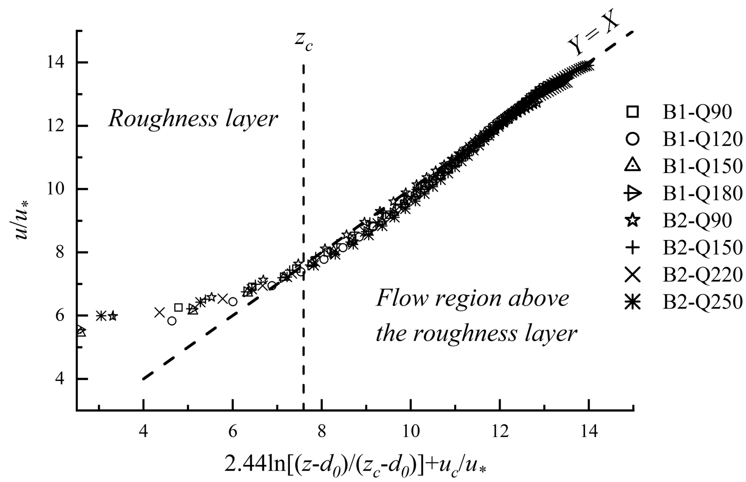

Fig. 18. SPH streamwise velocity profiles with logarithmic distribution above the roughness layer. The location of z_c is different for different test cases in the present plot scale, however its average is indicated by a vertical dashed-line to show its approximate position.

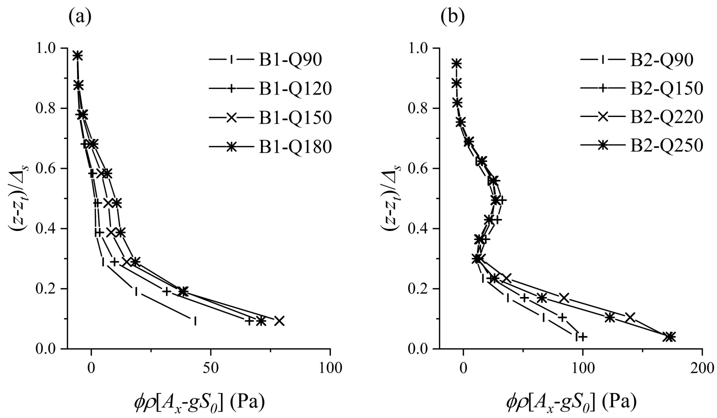

Fig. 19. Distribution of drag and gravity induced shear stress over the roughness layer.

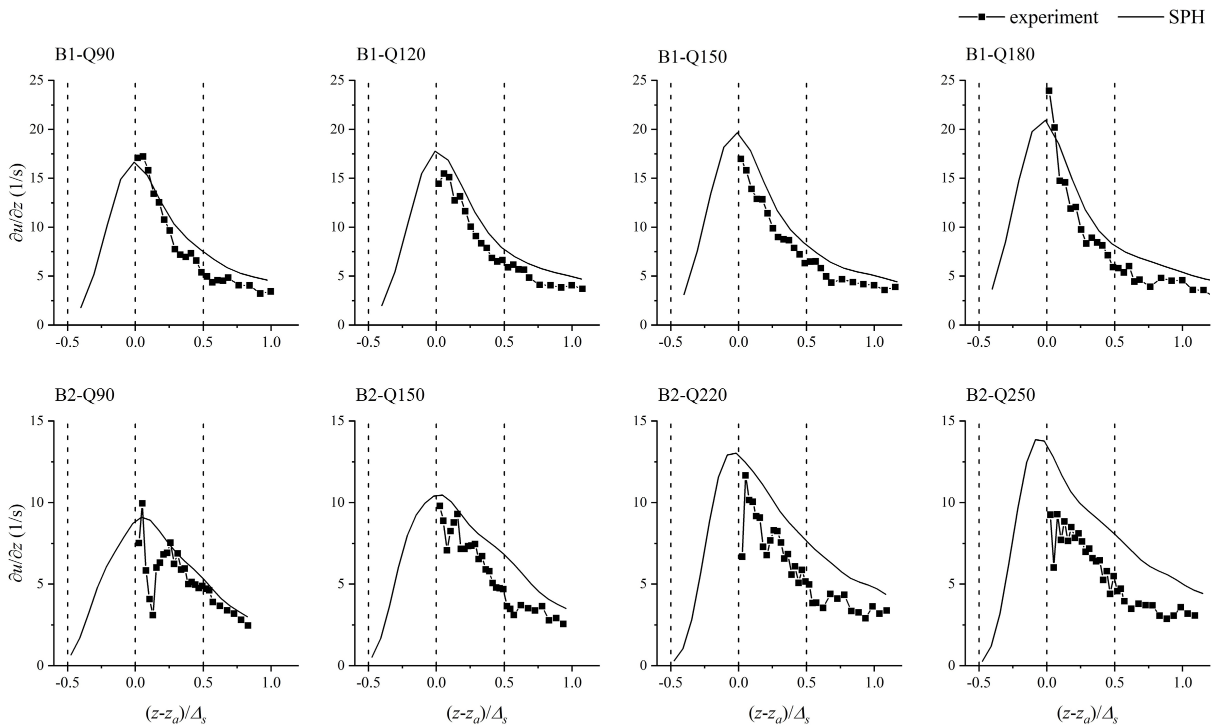

Fig. 20. Velocity gradients in the roughness layer. The dashed lines, from left to right, show the location of roughness trough z_t, centre of the roughness layer z_a, and roughness crest z_c. The experimental gradients are smoothed by applying a moving average procedure over three adjacent points, and those below z_a are not shown due to their large scatter.

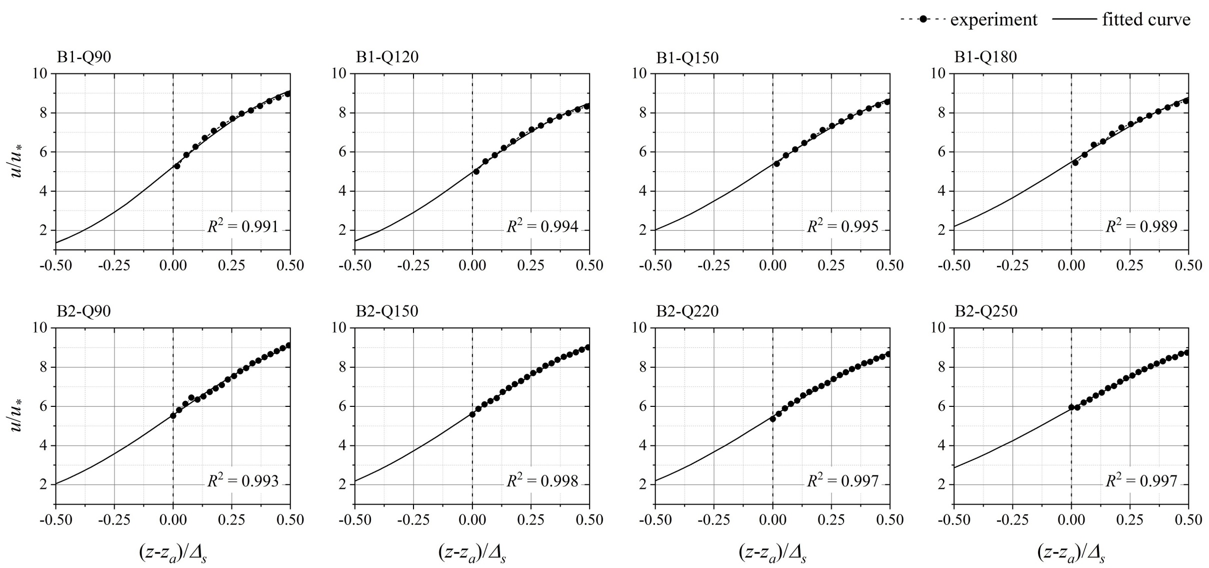

Fig. 21. Fitting sigmoid curves to the experimental velocity profiles within the roughness layer.

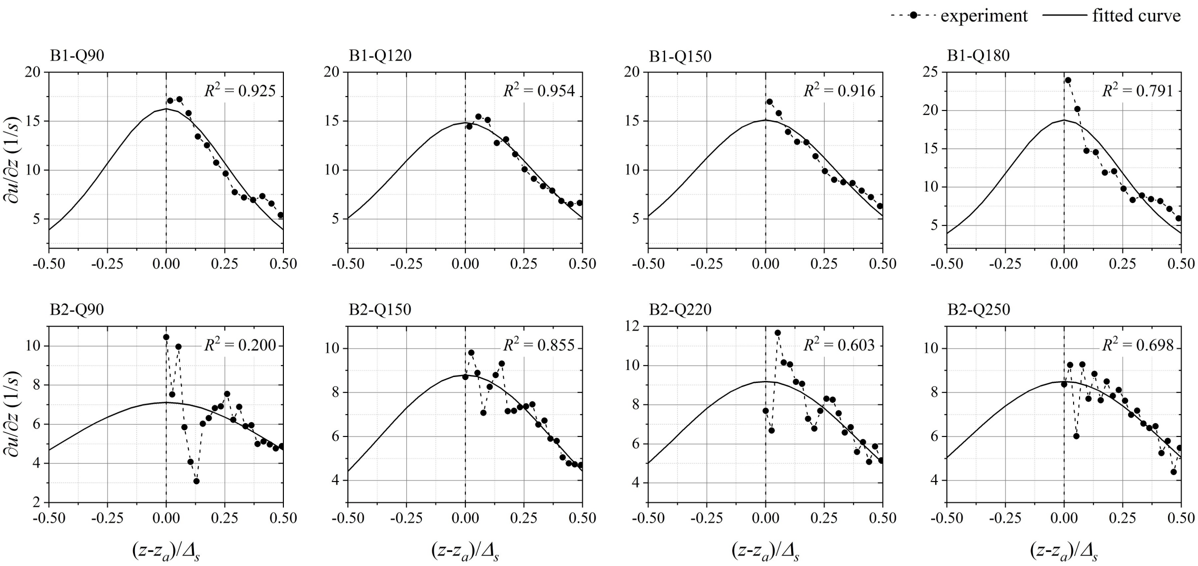

Fig. 22. Fitting sigmoid curves to the gradient of the experimental velocity profiles within the roughness layer.

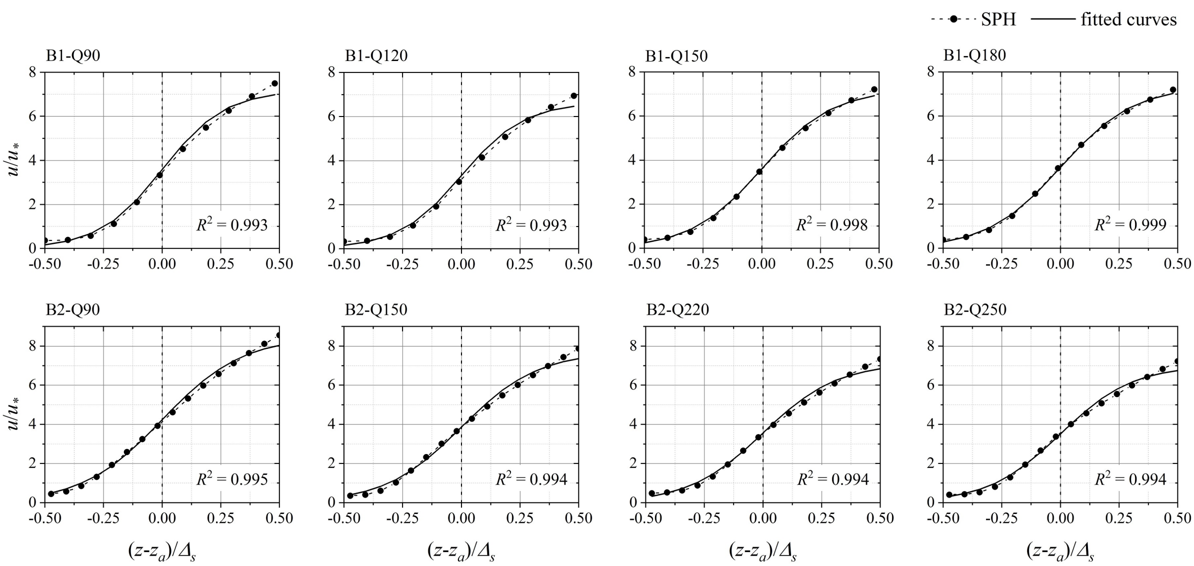

Fig. 23. Fitting sigmoid curves to the SPH-estimated velocity profiles within the roughness layer.

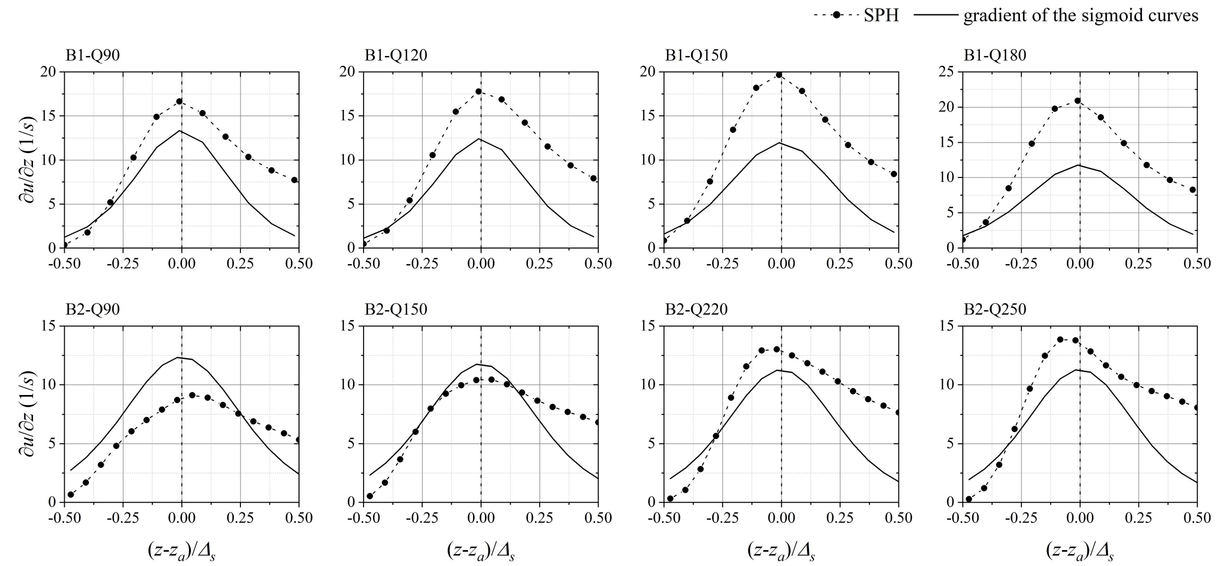

Fig. 24. Gradient of the sigmoid curves fitted to the velocity profiles in Fig. 23 in comparison with the SPH velocity gradients within the roughness layer.